Master’s Thesis of Engineering

# Multiphysics Modeling and Characterizing Melt Pool Formation during Laser-based Powder Bed Fusion (L-PBF) of Ti-6Al-4V

Ti-6Al-4V 재료를 사용한 레이저 분말 베드 용융법 (L-PBF)에서의 다물리 모델링 구축과 용융풀 특성화

February 2023

Graduate School of Aerospace Engineering
Seoul National University

Mingyu Chung

# Multiphysics Modeling and Characterizing Melt Pool Formation during Laser-based Powder Bed Fusion (L-PBF) of Ti-6Al-4V

Gunjin Yun

Submitting a master's thesis of
Engineering

February 2023

Graduate School of Aerospace Engineering
Seoul National University

Mingyu Chung

Confirming the master's thesis written by
Mingyu Chung
February 2023

| | | |
|---|---|---|
| Chair | Sangjoon Shin | (Seal) |
| Vice Chair | Gunjin Yun | (Seal) |
| Examiner | Howon Lee | (Seal) |

# Abstract

# Multiphysics Modeling and Characterizing Melt Pool Formation during Laser-based Powder Bed Fusion (L-PBF) of Ti-6Al-4V

Min Gyu Chung

Department of Aerospace Engineering

The Graduate School

Seoul National University

This thesis introduces a method for predicting melt pool morphology during L-PBF (Laser-Powder Bed Fusion) process using computational fluid dynamics (CFD). The L-PBF process is one of the promising additive manufacturing (AM) processes, which stacks layers by repeating laying micrometer-sized powders on the build plate, melting and solidifying them. Similar to other metal AM processes, the L-PBF process enables engineers to design and produce complex geometries more quickly than conventional manufacturing processes such as cutting and casting. Furthermore, it leaves much less waste. Despite of L-PBF's versatilities, manufactured parts still suffer from various defects such as lack-

of-fusion and keyhole. Analyzing the flow mechanisms in the melt pool is important to prevent these flaws, but it is complicated because of the extremely short time of the melting and solidifying process. Furthermore, distinct physical phenomena such as conduction, convection reflecting, evaporation, etc., are combined, which multiplies the complexity of investigating melt pool dynamics. To resolve this kind of problem, numerical simulation can be utilized. In this thesis, a multi-physics model for single-track/single-layer L-PBF is developed and used for evaluating the formation and evolution of melt pool with different processing parameters. The multi-physics model in this thesis considers phenomena such as multiphase flow, melting/solidification, conduction/convection heat transfer, capillary/thermo-capillary forces, recoil pressure, and material-dependent energy absorption. Also, this thesis mainly focuses on building a proper heat source model with a proper effective beam radius and energy absorptivity. The proposed simulation showed good agreement with the experimental results. Also, the numerical results presented that process parameters such as laser power and scan speed impacts significantly on the flows of molten metal and the formation of melt pool shape. As a result, the present study provides a better understanding of the mechanisms of flow dynamics in melt pools during the L-PBF process.

**Keyword** : Additive Manufacturing, Selective Laser Melting, Melt Pool Characterizing, Computational Fluid Dynamics

**Student Number** : 2021-27248

# Table of Contents

# List of Tables



# List of Figures

# Chapter 1. Introduction

## 1.1. Motivation

The additive manufacturing process is considered superior to the conventional manufacturing method because of the effectiveness of building complex designs, low material usage, and fast-manufacturing time with minimal post-processing. Although additive manufacturing including L-PBF has extraordinary potential to replace other manufacturing processes, the components produced by the additive manufacturing process still face numerous types of defects that deteriorate the parts' mechanical performance [1]. Voids, internal porosities, cracks, delamination, lack-of-fusion, dross, staircase effects, and warping are some of these defects [2, 3]. Process parameters such as scan speed, laser power, and hatch distance have a significant role in producing these defects[4, 5]. For example, low laser power intensity can lead to lack-of-fusion, and excessive heat input can make pores in the melt pool. Essentially, the flow pattern, which is affected by the process parameters, controls the melt pool's final morphology and the defects' generation. In this respect, it is necessary to understand the flow characteristics according to various process parameters.

As a way of investigating the thermal and fluidic characteristics of the melt pool, in-situ investigations can be used [6]. However, usage of in-situ monitoring systems is limited because of their high operating cost and lack of capability to observe complex physical phenomena precisely. The coexistence of various interactive

phenomena, such as capillary force, thermo-capillary force, recoil pressure, evaporation, laser reflection, recoil pressure, heat transfer (conduction, convection, and radiation), etc., present within microns and microseconds [7]. This short presence of physical phenomena makes it difficult to study the flow characteristics of the melt pool solely by means of experiments. However, building a precise numerical model that can reflect the physics during the L-PBF process could be an alternative way to study the melt pool dynamics.

As a result, in this thesis, the multi-physics model was constructed to investigate the formation and evolution of the melt pool during the single-layer/single-track L-PBF process of Ti-6Al-4V titanium alloy.

# Chapter 2. Backgrounds

## 2.1. Metal additive manufacturing

Additive manufacturing (AM) is one of the most advanced manufacturing processes for producing metallic products. Unlike conventional manufacturing processes which subtract unnecessary portions from bulk material, additive manufacturing processes add materials continuously to build whole parts. Typically, additive manufacturing methods are divided into powder bed fusion (PBF) and direct energy deposition (DED). The difference between two AM processes is the way of supplying powder and sintering metal powders. The PBF process spreads metal powders uniformly to specific area called build plate or bed. After this procedure, the laser selectively radiates a specific area which will be a layer of desired parts [8]. On the other hand, DED supplies powder through the moving nozzle and sintering them immediately after their release[9]. Although DED can provide much higher manufacturing speed, PBF can offer a high-resolution design which is advantageous for incarnating complex design practically. Therefore, PBF has been adopted by many companies, including EOS GmbH, Siemens, General Electrics, etc.

A simple schematic of a typical L-PBF machine is shown in Figure 1. Firstly, fine (typically 10-60 μm [10]) spherical metallic particles are distributed on a build plate (or base plate) by a controllable coating device which is called blade. The distributed powder forms a thin layer, and then the laser passes predefined

waypoints based on the data provided through CAD files. During laser scanning, irradiated powders are amalgamated by being sintered or fully molten. After processing the first layer, the build plate is laid down, and another layer of powder is spread on the previous layer. Afterward, the powder spreading and laser scanning are continued until the completion of final product building.

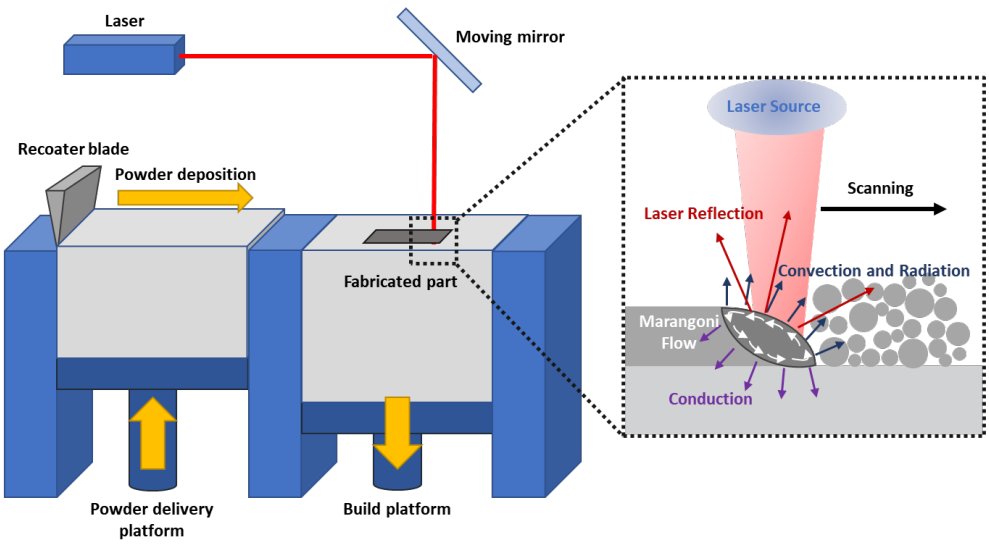


Figure 1. Schematic of Typical L-PBF Process

## 2.2. Melt Pool and Melting Modes

The melt pool is a part of the base material exposed to the heat source, molten and dented during the welding process. During the L-PBF process, the shape of the melt pool depends on the amount of energy input. With the redundant amount of energy, the material is vaporized and pushes the free surface of the melt pool so that depth of the melt pool becomes deeper. On the other hand, if low density of energy is applied to the surface of the material, the depth of the melt pool becomes shallow. The first one is called keyhole mode, and the

latter is called conduction mode.

In conduction mode, the heat conduction is the dominant heat transfer mechanism[11]. The cross-section of the melt pools in the conduction mode is generally semicircular so that the length of the melt pool depth is shorter or equal to half of the melt pool width.

On the other hand, in keyhole mode, the depth of the melt pool is controlled by the recoil pressure generated by the evaporation of the base material[12, 13]. Convective heat transfer due to thermo-capillary convection is dominating heat transfer mode in the melt pool. The top region of the melt pool in keyhole mode looks like an hourglass due to the outward flow by the Marangoni effect. In contrast, the bottom of the melt pool is much narrower than the upper region, which resembles the shape of a keyhole. Generally, the depth of the melt pool in the keyhole mode is greater than half of the melt pool width.

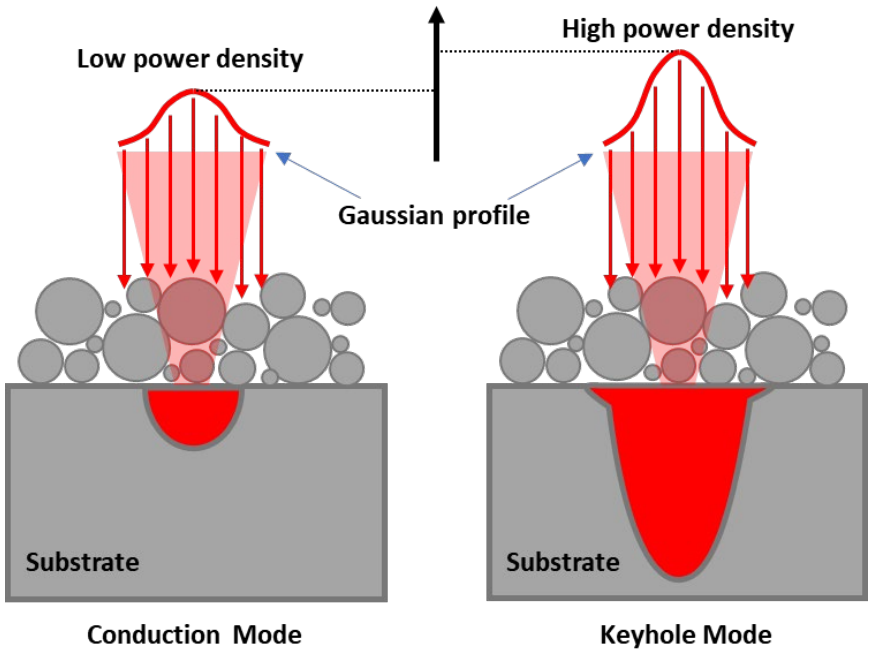


Figure 2. Conduction Mode and Keyhole Mode

## 2.3. Process Parameters

The quality of the additively manufactured products is highly dependent on the laser–material interactions determined by the combination of the process parameters. Typical process parameters in the L–PBF process are powder layer thickness, laser spot size, hatch distance, scanning speed, etc. Proper selection of the process parameters is vital to prevent defects such as pores, lack of fusion (LOF), surface roughness, microfractures, delaminated areas, and dimensional inaccuracies[5, 14, 15]. For example, increasing the laser power and decreasing the scanning speed, hatch distance, or layer thickness can lead to lower energy density, which produces defects like lack of fusion[16, 17]. Therefore, it is always important to establish suitable process parameters, but it is challenging activity.

Both experimental and numerical research are conducted to find out flawless processing conditions, recently.

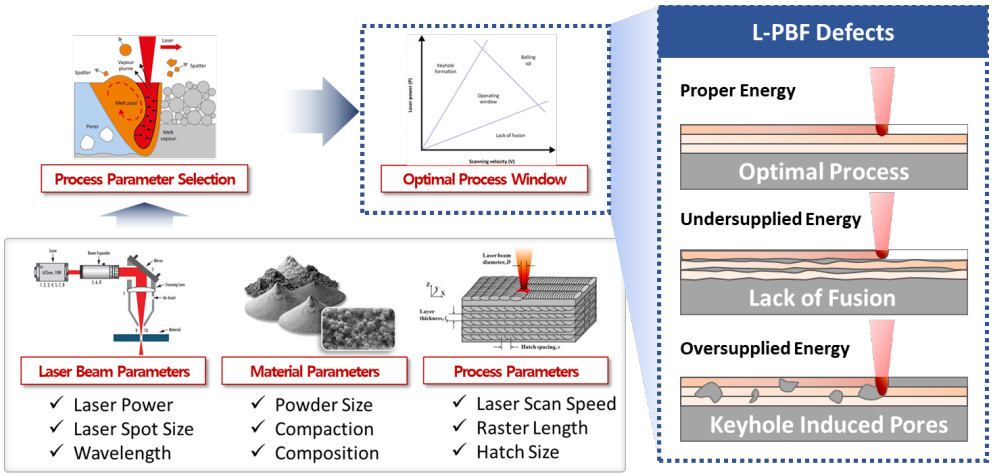


Figure 3. Process Parameters and Major Defects

## 2.4. Related Research

Due to the limitation of the experimental approach, there were many endeavors to build computational models for the analysis of the melt pool. The basic model considers only purely thermal approaches, which contains moving heat source for the estimation of the melt pool size and thermal histories are done by Bontha et al. [18, 19]. For the purposes of evaluating the residual stresses and deformation, the integration of the thermo-elasto-plasic modeling to the simple moving heat source was conducted by few researchers [20, 21]. Boley et al. [22] investigated the transmission of the laser powder bed and revealed that the substrate only absorbs small portion of the laser energy. According to their research, the absorption rate of the surface and the inside of the powder layer is different. Therefore,

they insisted that the different energy inputs with different positions of the powder layer should be considered when developing a heat source in the simulation. Qiu et al. studied the effect of laser scanning speed on porosity with their CFD model [23]. They also used heat source as volumetric heat source.

Some researchers focused on the flow characteristics of the melt pool. For example, Khairallah and Anderson made a high-resolution numerical model of an L-PBF process of 316L stainless steel [24]. In their research, the effect of the surface tension on the melt pool morphology was investigated. However, they neglected some thermo-coupled physics such as the presence of recoil pressure, and thermo-capillary force. Since they did not consider those physics in their model, they have to maintain the energy level of the laser not to enter the keyhole mode. As a result, Khairallah et al. their model proposed in new research reflected the Marangoni effect and the recoil pressure [16]. More complex model with double track with the nickel alloy was modeled by Lee and Zhang [25]. Their model was built using the finite volume method (FVM) to analyze the melt pool geometry and the grain morphology of a double track L-PBF process. In their model, the multiple reflection model was included to simulate precise laser-material interaction. However, the melt pool regime was still in the stable conduction mode with relatively low heat input.

Large number of previous research used simplified models such as volumetric heat source, neglecting surface tension changes, and recoil pressure. Also, they did not consider the powder which might alter the reflection characteristics.

# Chapter 3. Model Descriptions

During the L-PBF process, due to its relatively high level of power concentration on a small surface area, metal powders and substrates melt in an instant and even evaporate sometimes. In the such region, physical phenomena such as recoil pressure, capillary and thermo-capillary forces are prevalent and rule the molten metal's flow behavior. Since the sintering process occurs at a moment, it is required to build a numerical model solving mass, momentum and energy conservation equations together. In this thesis, commercial CFD software Flow-3D was used to solve these equations all at once. Moreover, the ray-tracing method was implemented to depict the interactions between laser rays and the material including powder, and substrate in both phases (solid and liquid). In the following sections, the governing equations and models for laser-material interaction used in this thesis are introduced.

In this study few assumptions are made for the CFD model; ① flow in melt pool is incompressible, viscous, laminar, ② shear stress is linearly proportional to velocity gradient (Newtonian fluid), ③ powders are considered as static during the process, so that no particles are floating on the melt pool, ④ generation of fume and its affection on laser beam are neglected, ⑤ spattering of material is not considered.

## 3.1. Fluid Flow and Heat Transfer Model

### 3.1.1. Fluid Flow Model

The computational domain in the CFD model is composed of two different phases. The first phase is the ambient air, and the second is the metal region. Since two phases are immiscible, it is important to track the interface between air and metal. In this thesis, the volume of fluid (VoF) method is used to track the free surface.

$$\frac{1}{\rho_q}\left[\frac{\partial}{\partial t}(\alpha_q \rho_q) + \nabla \cdot (\alpha_q \rho_q \mathbf{u})\right] = 0 \quad (1)$$

In the equation (1) $\mathbf{u}$ is the velocity vector and $q$ is the phase indicator which represents the air and metal respectively. For the volume fraction equation, the summation of the volume of all phases should be equal to unity.

$$\alpha_F + \alpha_V = 1 \quad (2)$$

where the subscript $F$ denotes fluid phase (metal) and $V$ denotes void phase (air) respectively.

The properties appearing in the transport equations are calculated by the volume fraction of secondary phases in each control volume. In the two-phase multiphase flow, for example, the density can be calculated as expressed in equation (3).

$$\rho = \alpha_V \rho_V + (1 - \alpha_V)\rho_F \quad (3)$$

Other properties such as viscosity can be computed in same manner.

To determine the pressure-velocity field, a single momentum equation is solved. The momentum equations which is dependent on the resultant properties of all phases are:

$$\frac{\partial}{\partial t}(\rho u)+\frac{\partial}{\partial x}(\rho uu)+\frac{\partial}{\partial y}(\rho vu)+\frac{\partial}{\partial z}(\rho wu)=-\frac{\partial P}{\partial x}+F_x \quad (4)$$

$$\frac{\partial}{\partial t}(\rho v)+\frac{\partial}{\partial x}(\rho uv)+\frac{\partial}{\partial y}(\rho vv)+\frac{\partial}{\partial z}(\rho wv)=-\frac{\partial P}{\partial y}+F_y \quad (5)$$

$$\frac{\partial}{\partial t}(\rho w)+\frac{\partial}{\partial x}(\rho uw)+\frac{\partial}{\partial y}(\rho vw)+\frac{\partial}{\partial z}(\rho ww)=-\frac{\partial P}{\partial z}+F_z+F_g \quad (6)$$

$(u,v,w)$ are the components of velocity vector **u** in x, y and z directions, and $F$ terms are stand for the viscous stress. The viscous stress can be defined as:

$$F=\nabla\left[\mu(\nabla \mathrm{u}+\nabla \mathrm{u}^T)-\frac{2}{3}\mu(\nabla\cdot \mathrm{u})\delta\right] \quad (7)$$

Since the flow is assumed to be incompressible, the last term in the above equation can be eliminated.

Also, the last term on the right-hand side of Equation (6) is for the buoyancy force acting on the fluid. According to temperature change, the molten metal's density changes because of thermal expansion and buoyancy forces are generated. In this thesis, the Boussinesq approximation is used for calculating buoyancy force due to the incompressibility of the fluid.

$$F_g = \rho g \beta (T - T_l) \tag{8}$$

where $\beta$ is the thermal expansion coefficient of metal and $T_l$ is the liquidus temperature of the metal.

### 3.1.2. Heat Transfer Model

To evaluate the temperature field and the phase change condition, the energy conservation equation should be coupled to the velocity and solved together. The energy equation for the computational domain is:

$$\rho \left[ \frac{\partial h}{\partial t} + (u \cdot \nabla) h \right] = \nabla \cdot (k \nabla T) \tag{9}$$

where $h$ is the enthalpy and $k$ is the thermal conductivity of the metal. The enthalpy of fluid(metal) can be described as:

$$h = h_{ref} + c_{p,bulk}\left(T - T_{ref}\right) + f_l \Delta H_{sl} \tag{10}$$

$$f_l = \begin{cases} 0 & T < T_s \\ \dfrac{T - T_s}{T_l - T_s} & T_s \le T < T_l \\ 1 & T_l < T \end{cases} \tag{11}$$

In the above relationship in Equation (9), $c_{p,bulk}$, $\Delta H_{sl}$ and $f_l$ are specific heat capacity, latent heat of fusion and liquid fraction function respectively. By rule of mixture, $c_{p,bulk}$ is:

$$c_{p,bulk} = \frac{\alpha_F \rho_F c_{p,F} + \alpha_V \rho_V c_{p,V}}{\alpha_F \rho_F + \alpha_V \rho_V} \tag{12}$$

Due to the high energy source, in the melt pool, various heat transfers including radiation, conduction, convection and phase change occur. To implement these physical phenomena into the equation, the following thermal boundary conditions are made.

$$-k\frac{\partial T}{\partial n} = q''_{rad} + q''_{conv} + q''_{evap} + q''_{laser} \tag{13}$$

$$q''_{rad} = \varepsilon\eta(T^4 - T^4_{surr}) \tag{14}$$

$$q''_{conv} = h(T - T_{surr}) \tag{15}$$

$$q''_{evap} = \frac{\Delta H_{lv} \cdot A_{accom}}{\sqrt{2\pi R_v T}}\left[P_{atm}\exp\left\{\frac{\Delta H_{lv}}{R_v T_{boil}}\left(1 - \frac{T}{T_{boil}}\right)\right\}\right] \tag{16}$$

$$q''_{laser} = q_{focus}\exp\left(-2\frac{r^2}{r_b^2}\right) \tag{17}$$

$\varepsilon$ and $\eta$ are emissivity and Stefan–Boltzmann constants, respectively. $\Delta H_{lv}$, $T_{boil}$, $R_v$ are the latent heat of evaporation, boiling temperature, and gas constant of the vaporized metal. Details of Equation (16) and (17), equations for the volumetric heat sink due to the evaporative cooling and heat input due to laser source, will be explained in the following sections.

## 3.2. Heat Source Model

There were several attempts to model the effect of the laser on the thermal behavior of the material, for example, moving point

source, moving heat flux, moving volumetric heat source, etc. Among these approaches, the ray-tracing method has a great advantage on the mimic the actual physics of laser behavior during melt pool generation. By using the ray-tracing method, the heat flux emitted from the laser radiates the surface of the metal region and gives some portion of its energy. Then, lights reflected with the remaining energy and radiates another surface encountered. During this process, the energy distribution of the laser beam is assumed to have a planar Gaussian-like distribution due to the laser optical physics. As Figure 4, the typical laser source has a certain focused/defocused zone and shows Gaussian-like axisymmetric energy distribution at the focused area. The distribution equation of energy density can be expressed with the radial coordinate of the laser ($r$) and the position of the inflection point ($r_b$) and the heat density value at the beam center. The established energy density equation is described as same as Equation 17:

$$q''_{laser} = q_{focus}\exp\left(-2\frac{r^2}{r_b^2}\right) \quad (17)$$

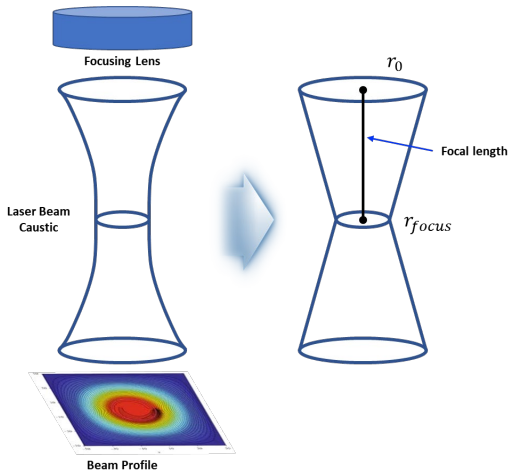


Figure 4. Typical Cone Shape Beam Profile

Depending on the resolution of the computational domain, the analytical expression of the laser energy density will be digitized into a finite number of smaller parts while keeping its total energy value. An example of discretized energy distribution is shown in Figure 5.

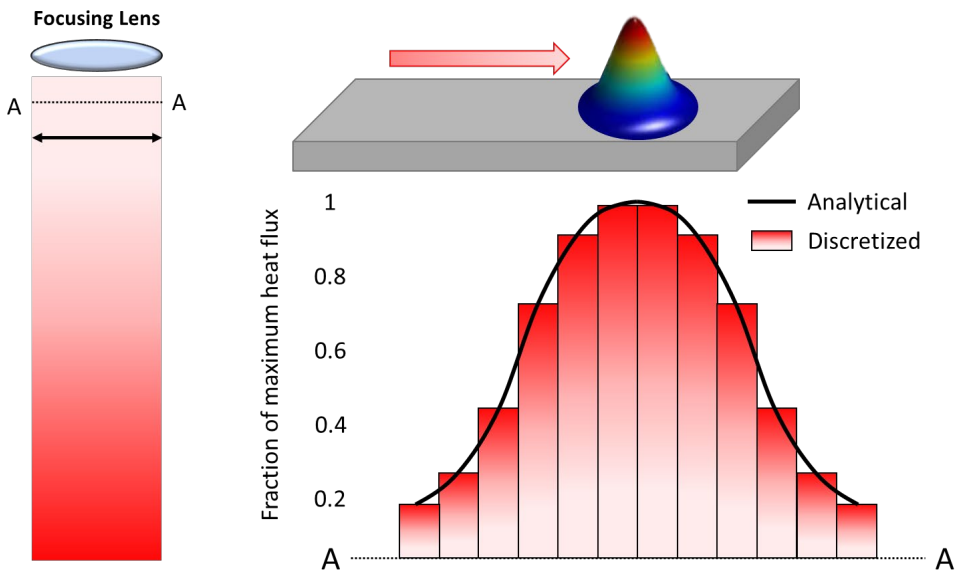


Figure 5. Gaussian Distribution Profile of Laser Power

Since the energy from the laser beam is dispersed to discrete cells, the accuracy of the energy dispersion is determined by the

resolution of the mesh. Moreover, this accuracy directly affects to the calculation of temperature, recoil pressure and consequently the flow behavior. Therefore, it is recommended to refine the mesh enough, so that the energy distribution of the laser beam is accurately represented on discrete cells.

In this thesis, 8 μm−sized cells which have relatively good resolution to capture the energy distribution and economic computational cost were used. The laser spot radius for the model was 60 μm, which has 42.4 μm of effective beam radius. The overall Gaussian−like energy distribution profile is shown is Figure 6.

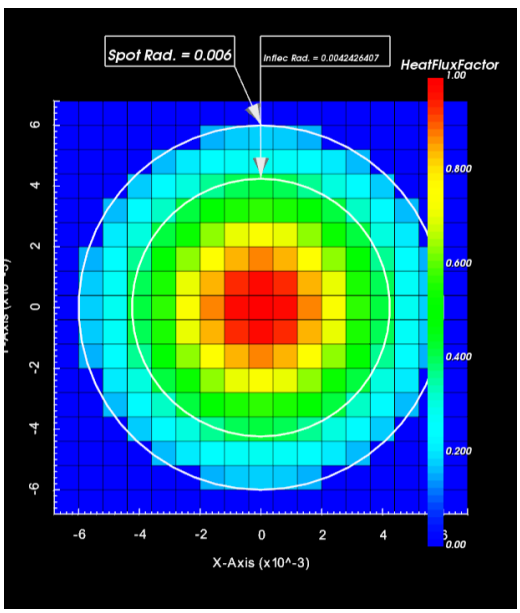


Figure 6. Gaussian Source Modeled in Simulation

Based on the energy distribution profile and the computational cell sizes, the rays will be formed. According to the laser setting such as power and position, each laser ray moves forwards maintaining its initial direction $\vec{e}_{ij}$ with its power $Q_{ij}$. If the ray arrives at certain cells containing free surface of the fluid, the new direction of the

reflected ray is calculated as:

$$\vec{e}_{i,j+1} = \vec{e}_{i,j} - 2(\vec{e}_{i,j} \cdot \vec{n}_{i,j})\vec{n}_{i,j} \quad (18)$$

In Equation (18), $i$ will be unchanged during the calculation because it is for the tag of each laser ray. On the other hand, $j$ indicates the number of collisions with the free surface of the fluid.

At the same time tracking laser ray reflection, the updating of level of the energy for each laser ray is conducted after each collision. When the $i^{th}$ ray which contains the initial energy of $Q_{ij}$ hit the free surface, a certain amount of its initial energy is transferred to the fluid. The remaining amount of laser energy, then, carried away with the reflected ray with the vector of $\vec{e}_{i,j+1}$.

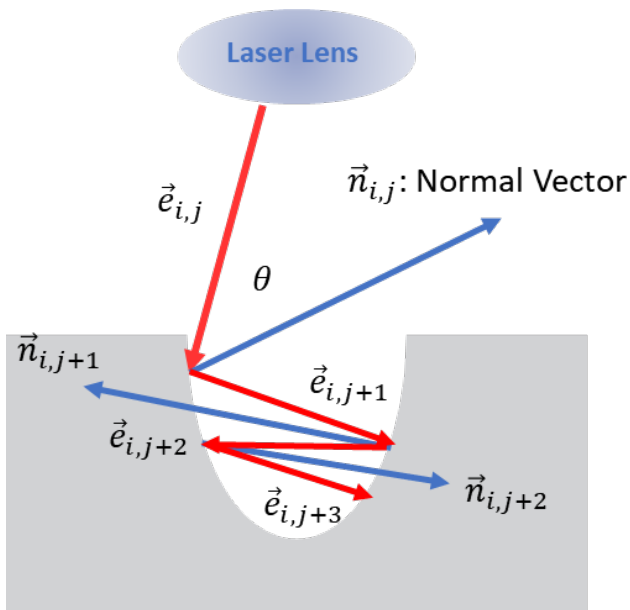

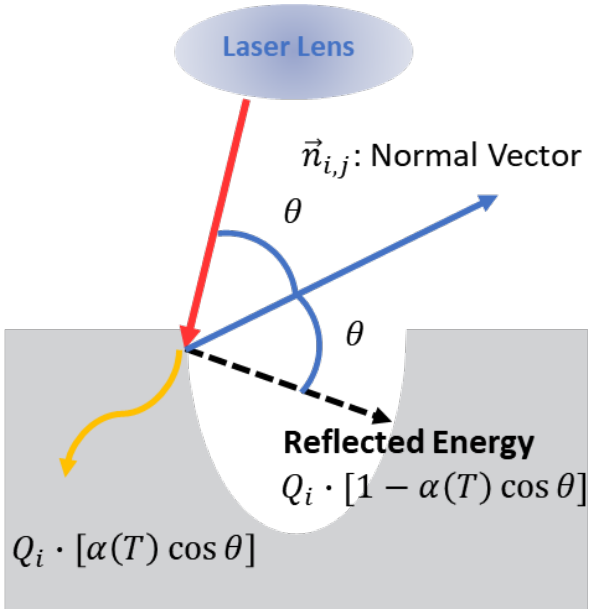


Figure 7. Reflection and Ray-tracing in the Melt Pool

The amount of energy absorbed by the fluid is determined by the local absorptivity of the fluid. The absorptivity of energy is highly dependent on the incident angle. In this thesis, the Fresnel reflection model which is widely accepted for the calculation of the laser absorption rate was adopted. In the Fresnel reflection absorption model, the absorption rate $a$ can be expressed with the incident angle and the material-dependent electrical conductance coefficient $\varepsilon$.

$$a = 1 - \frac{1}{2}\left(\frac{1 + (1 - \varepsilon\cos\theta)^2}{1 + (1 + \varepsilon\cos\theta)^2} + \frac{\varepsilon^2 - 2\varepsilon\cos\theta + 2\cos^2\theta}{\varepsilon^2 + \varepsilon\cos\theta + 2\cos^2\theta}\right) \quad (19)$$

The value of $\varepsilon$ is determined from the material properties such as relative permittivity of base material and plasma, the permittivity of vacuum, and electrical conductance per unit depth of metal. However, for a certain laser type, rough values of $\varepsilon$ are determined already.

For steel with a $CO_2$ laser, it is recommended to use the value of 0.08 [26]. Additionally, for the Nd: YAG laser, the suggested value of $\varepsilon$ is 0.25 [26]. In this thesis, the $\varepsilon$ was varied from 0.12 to 0.20 according to the laser power.

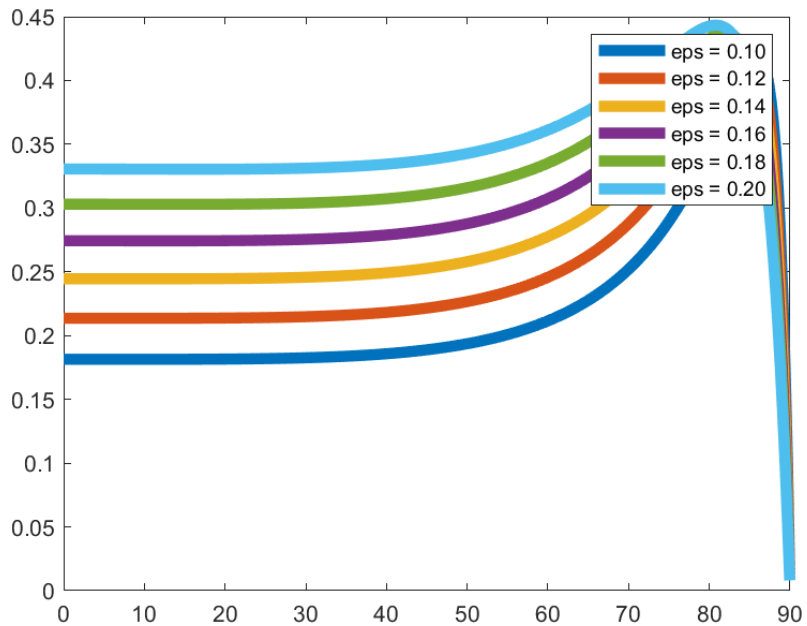


Figure 8.Absorptivity of the Fresnel reflection model according to the electrical conductance coefficient and the incident angle in radian

## 3.3. Recoil Pressure and capillary forces

Due to the high energy density of the heat source, imposed heat fluxes rise the temperature of the base material (substrate and powder), and the elevated temperature makes the material boil and evaporate. When the vaporization occurs, the negative force is generated acting on the fluid's free surface, which is called recoil pressure. This force depresses the molten metal and excessive forces generate defects called keyholes. Also, the concentrated high

temperature leads to large temperature gradients, which intensifies the thermally induced shear stress on the fluid. Furthermore, the final morphology of the melt pool is determined by the surface tension during the cooling process.

Three major forces acting on the free surface of the melt pool can be described as:

$$\tau_{recoil} = 0.54 P_{atm} exp\left[\frac{\Delta H_{lv}}{R_v T_{boil}}\left(1 - \frac{T_{boil}}{T}\right)\right]\vec{n} \quad (20)$$

$$\tau_{capillary} = \left(\sigma_{ref} - \gamma\left[T - T_{ref}\right]\right)\kappa \quad (21)$$

$$\tau_{Marangoni} = \gamma\left[\vec{\nabla}T - \left(\vec{\nabla}T \cdot \vec{n}\right)\vec{n}\right] \quad (22)$$

where $\Delta H_{lv}$ is the latent heat of vaporization and $R_v$ is the vaporized metal gas constant again. $\sigma_{ref}$ and $\gamma$ expressed in Equations (21) and (22) are the reference surface tension and the sensitivity of surface tension with respect to temperature, respectively. Also, $\kappa$ is the curvature of the surface of liquid metal.

## 3.4. Powder Lay

To obtain the distribution of the powder on the build plate, the discrete element method (DEM) was adopted. DEM can depict the physics between colliding particles, which is suited for tracking the position of a large number of powders. The free-body diagram of two colliding particles is shown in Figure 9.

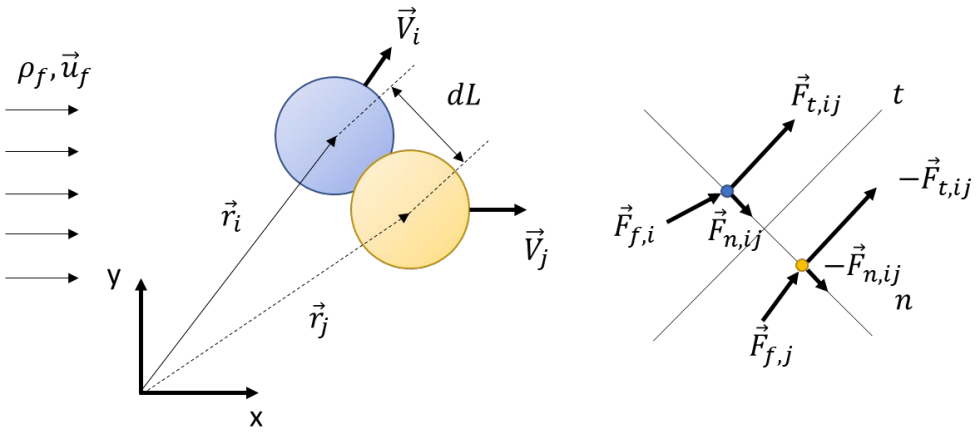


Figure 9. Free Body Diagram of Two Colliding Particles

Forces acting on the particles can be calculated using Hertz and Voigt models.

$$\vec{F}_{n,ij} = -[k_n \cdot (dL)]\vec{n}_{i,j} - \eta_n[\overrightarrow{\Delta V}_{i,j} \cdot \vec{n}_{i,j}]\vec{n}_{i,j} \tag{23}$$

$$\vec{F}_{t,ij} = -\eta_t[\overrightarrow{\Delta V}_{i,j} - (\overrightarrow{\Delta V}_{i,j} \cdot \vec{n}_{i,j})\vec{n}_{i,j}] \tag{24}$$

$$\vec{F}_{f,i} = -\frac{1}{2}C_D(Re)|\vec{V}_i - \vec{u}_f|^2 \frac{(\vec{V}_i - \vec{u}_f)}{|\vec{V}_i - \vec{u}_f|} \tag{25}$$

$$\vec{F}_{tot,i} = \vec{F}_{n,ij} + \vec{F}_{t,ij} + \vec{F}_{f,i} \tag{26}$$

Subscript $n$ is for the normal direction and $t$ is for the tangential direction. $k$ and $\eta$ are the effective spring coefficient and damping coefficient based on the Voigt model, respectively. $\vec{n}_{i,j}$ is the vector connecting the center of mass of the $i$ and $j$ particles. Equation (25) is the force acting on particles due to the viscous drag.

The size of the normal and tangential force acting on two colliding

particles are same. On the other hand, the direction is opposite. As described in Equation (26), the total force acting on each particle is the summation of 3 different forces.

The effective spring coefficient and damping coefficients can be expressed as [59, 60, 61, 62]

$$k_n = \frac{\sqrt{3}}{3(1-\nu)}E \tag{27}$$

$$k_t = \frac{\sqrt{3}(1-3\nu)}{3(1-\nu^2)}E \tag{28}$$

$$\eta_n = 2\sqrt{mk_n} \tag{29}$$

$$\eta_t = \eta_n(k_t/k_n)^{1/4} \tag{30}$$

$E$ is the Young's modulus and the $\nu$ is the Poisson's ratio of particle.

## 3.5. Materials and Thermophysical Properties

Titanium alloy is one of the most widely used materials for metal additive manufacturing. The alloy Ti-6Al-4V is one of this kind which has an excellent combination of specific mechanical properties. Ti-6Al-4V has low weight and outstanding corrosion behavior, so that this alloy is suitable for high-performance applications in the aerospace industry. Considering these characteristics, Ti-6Al-4V was chosen for the material used in this thesis.

The following table contains the thermophysical properties applied to the proposed model.

Table 1. Ti-6Al-4V Thermophysical Properties [7, 27]

| Property | Value | Property | Value |
|---|---|---|---|
| $T_s$ | 1873.15 K | $C_{p,s}$ | 546 J/kg/K |
| $T_l$ | 1923.15 K | $\rho$ | 4420 kg/m$^3$ |
| $T_{boil}$ | 3315 K | $\mu$ | 0.00325 Pa.s |
| $T_{surr}$ | 300 K | $R_v$ | 195 J/kg/K |
| $\Delta H_{sl}$ | 286 kJ/kg | $\Delta H_{lv}$ | 9.7 MJ/kg |

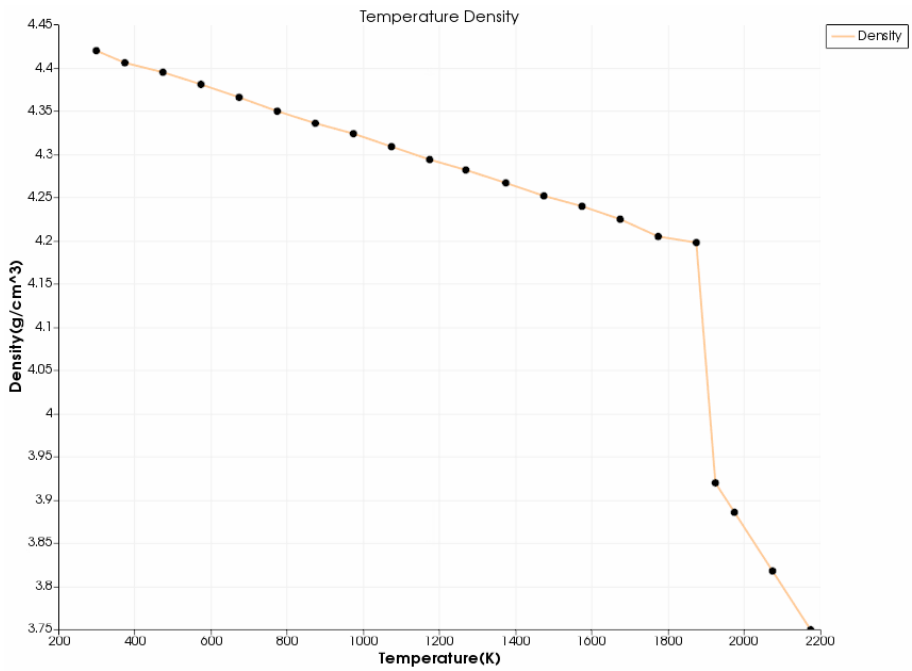


Figure 10. Density Change with Different Temperature

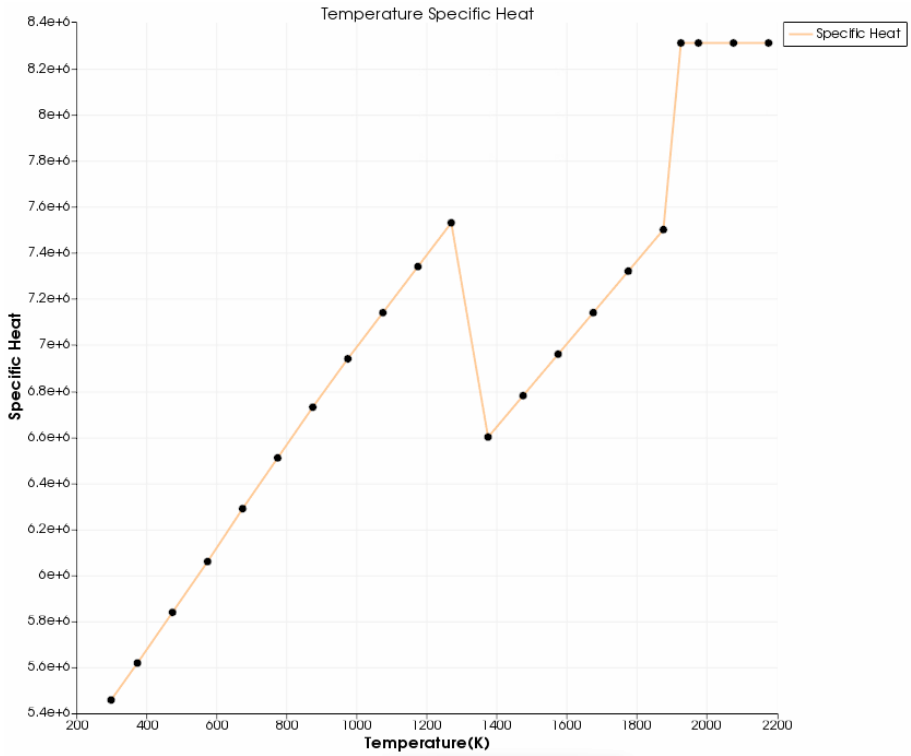


Figure 11. Specific Heat Change with Different Temperature

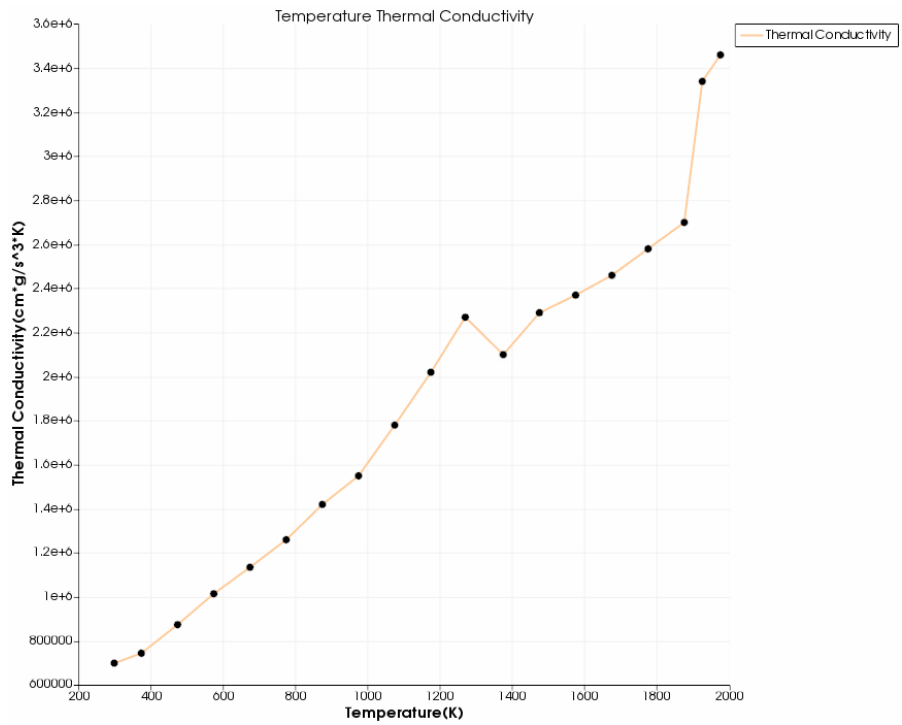


Figure 12. Thermal Conductivity Change with Different

Temperature

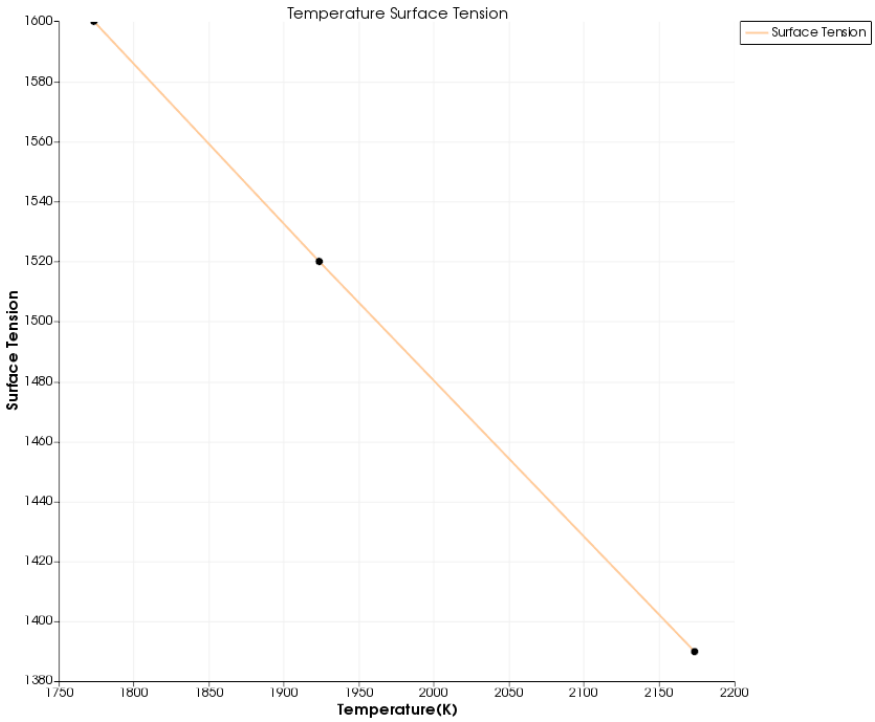


Figure 13. Surface Tension Change with Different Temperature

## 3.6. Model Establishment in Simulation

Total of 16 lines of single track were made on a bulk material of Ti-6Al-4V without powder. Every single track has different process parameters of scan speed and laser power. Since the layer with powders that have diameters smaller than around 50 μm has negligible effect on the morphology of melt pool[28], no powder simulations were carried out first, for the calibration purpose.

After the computing of single-track/single-layer L-PBF processes, 4 single tracks with powder model were simulated and compared with the results without powder.

### 3.6.1. Model without Powder

The domain size of the bulk Ti-6Al-4V is 1600μm×300μm×250μm. The top part of the domain is empty for gaseous air while the rest of the domain is covered with titanium alloy. For saving computational time, the symmetrical model was utilized. Therefore, except for the symmetric plane, all of the side panels of the domain are insulated as an adiabatic wall. The bottom boundary, also, is set to be adiabatic wall. In contrast to the bottom wall, the top boundary is set to be open and has specified pressure value. In this model, the top area has constant pressure of 1 atm and the temperature of room temperature. The starting point of the laser is 200 μm apart from the adiabatic wall and moves toward the opposite side of the wall. The length of the track is 1400 μm. The cell size of the domain is 8 μm which has both relatively fast computational speed and accuracy in capturing laser energy distribution and surface morphology. The total number of cells is 380,000 for all models without power. The processing parameters used in this simulation are the combination of different laser power (50W, 100W, 150W, and 195W) and scan speed (500mm/s, 750mm/s, 1000mm/s, and 1200mm/s). The computational time for these problems varies from 4 to 12 hours according to process parameters on a 48-core workstation with two Intel Xeon Gold 6248R 3.0GHz CPU and 256GB RAM.

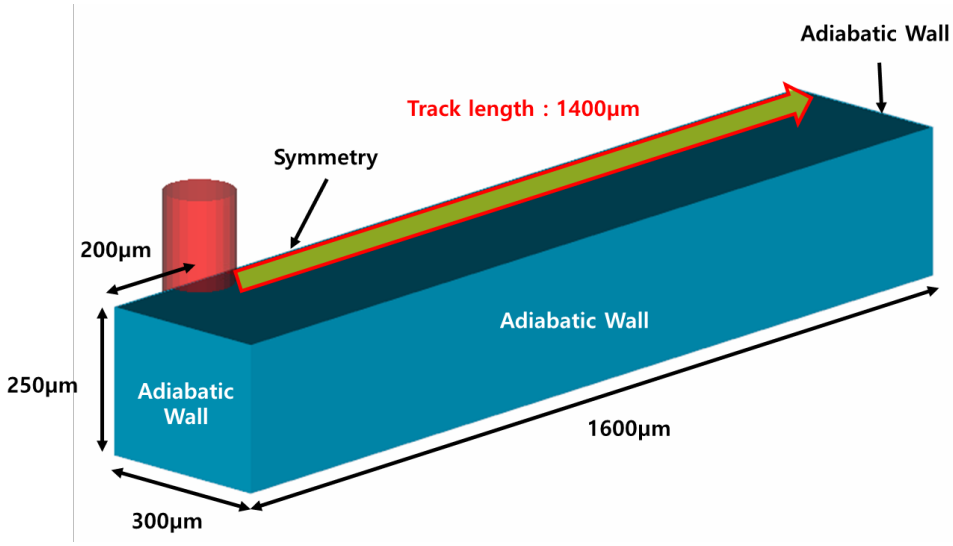

Figure 14. 3D View of the Computational Domain without Powder

### 3.6.2. Model with Powder

Although it is known that the morphology of the melt pool is unchanged when the powder particles' diameter is lesser than about 50 μm, the simulation with the powder is needed to reflect the complex laser-powder interaction on the flow. Furthermore, precise morphology tracking is available as well as the transient state of fluid flow in the melt pool during the L-PBF process.

The surface morphology of the initial powder layer can be reproduced by using DEM simulation. In this thesis, Flow-3D DEM module was utilized for powder model establishment with true particle size distribution. Typical powders used for the additive manufacturing have Gaussian-like diameter distribution as shown in Figure 15. This paper employed powder diameter distribution based on the research conducted by Liang et al [29] and the layer thickness of 30 μm to compare the result proposed by Dezfoli et al [30]. The

particle size distribution was discretized into 9 different particle sizes including 15, 20, 25, 30, 35, 40, 45, 50, and 55 μm. With this information and the mechanical properties of Ti-6Al-4V, the spreading process was simulated to determine the initial distribution of the powder particles. Then, the final distribution of the particle was obtained by simulating the spreading process with the moving blade. The whole process written above is shown in Figure 15.

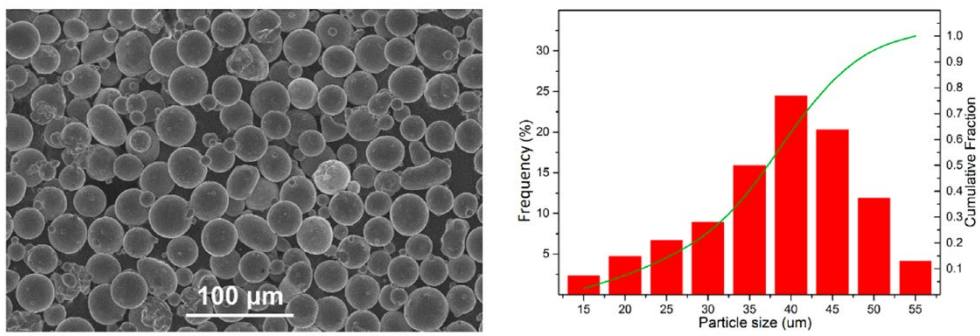


Figure 15. SEM Image of the Powder & the Powder Size Distribution [29]

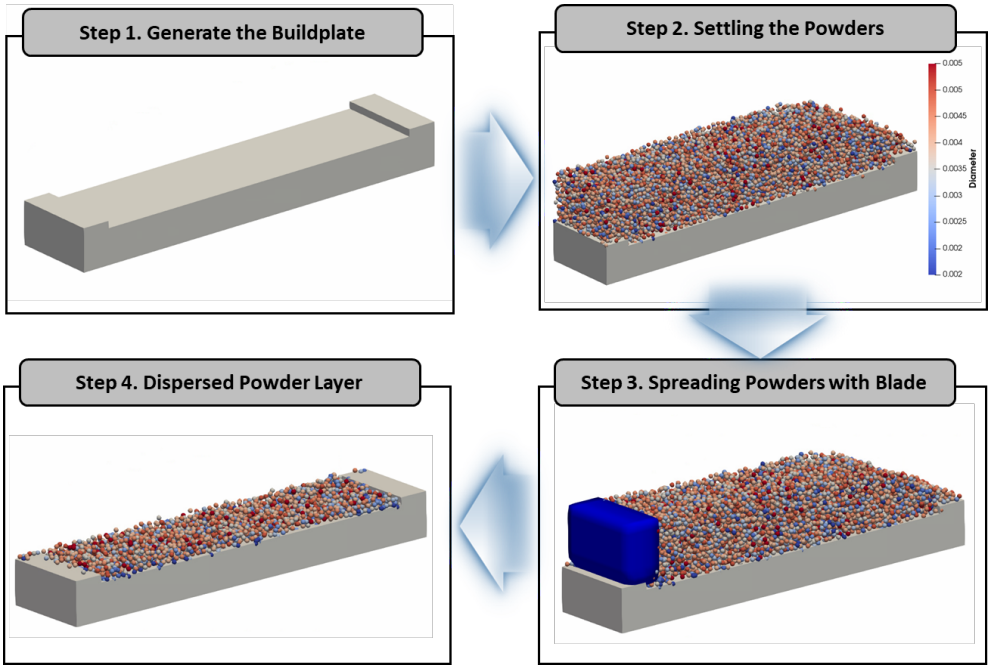


Figure 16. Particle Spreading Simulation using DEM

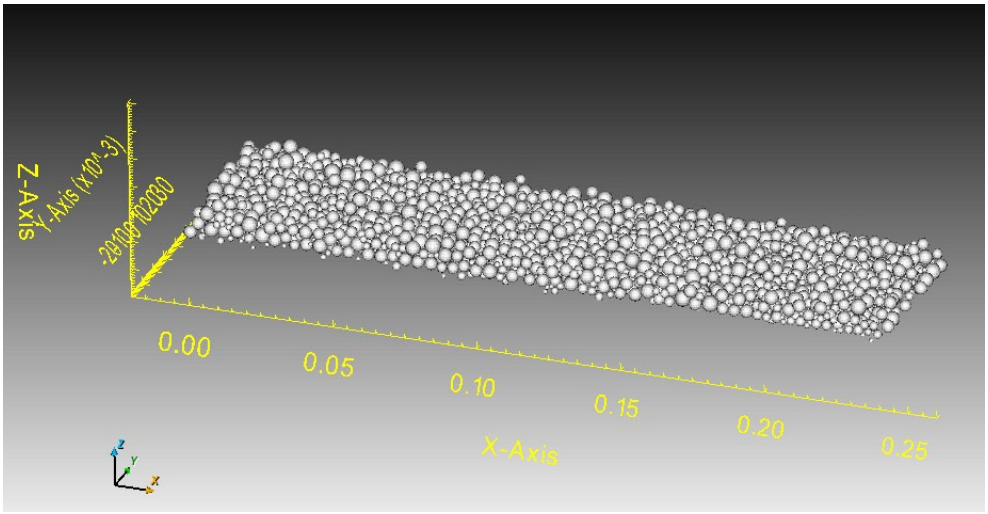


Figure 17. Generated Layer Geometry with Powder

The domain size for the simulations with powder is 2200μm×1200μm×250μm. For the purpose of increasing the stability of the simulation, the buffer volume called thermal diffusion block was added, so that the domain size is much larger than the previous bulk material L-PBF process simulation. Although the domain size was changed, the boundary conditions remain almost same. The top part of the domain is empty for the gaseous state of air and the rest of the part is filled with metal. The bottom boundary is, again, set to be an adiabatic wall and the top boundary is open with 1 atm pressure. In contrast to the bulk simulation, in simulations with powders, symmetry boundary condition is not used because of the geometric asymmetry due to the presence of powders. Therefore, all the side planes are regarded as adiabatic walls.

The starting point of the laser is now adjusted to be 300 μm apart from the wall. The total length of the laser path is 1600 μm. The size of cells used is still 8 μm, which leads to 1,406,250 cells. Due to excessive running time, only a restricted number of conditions are adopted for the simulation. 4 different simulations with different laser power (50W, 100W, 150W and 195W) having same scanning speed (500mm/s) were calculated. The computational time for the powder problem varies from 13 to 37 hours on a 48-core workstation with two Inter Xeon Gold 6248R 3.0GHz CPU and 256GB RAM.

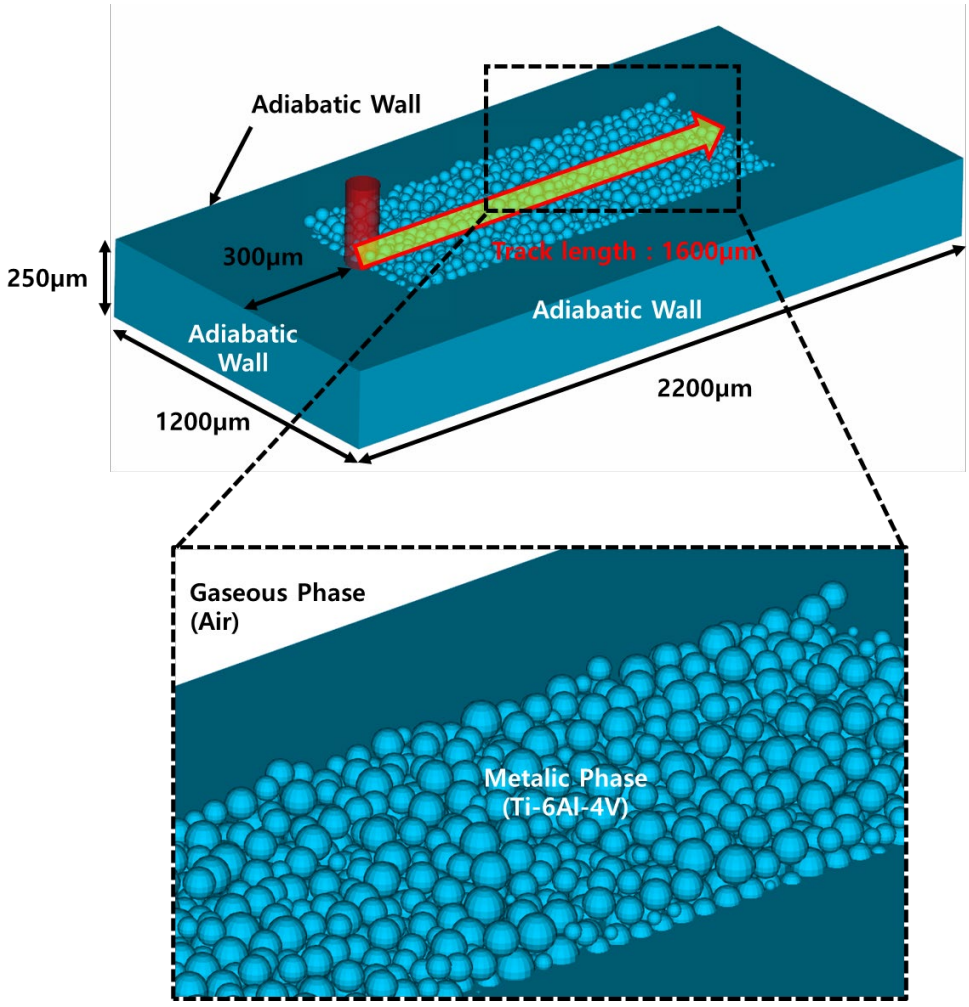


Figure 18. 3D View of the Computational Domain with Powder

# Chapter 4. Results and Discussion

It is well known that the process parameters such as laser power and velocity of scan collectively determine the heat input. Moreover, the heat input regulates the temperature distribution and fluid flow in the melt pool, which, in turn, affects the formation of the melt pool and surface morphology. Therefore, reversely, by evaluating both the geometry and surface morphology of the melt pool for each processing conditions, the interaction between the temperature distribution and fluid flow can be identified. In this thesis, L-PBF simulation without powder was conducted first to calibrate the physical properties including the laser energy absorptivity and effective beam radius. After calibration, the interaction mechanism and the flow in the melt pool were investigated in detail.

## 4.1. Geometry and Morphology of the Melt Pool without Powder

It is important to validate the simulation results and the experimental results to improve the reliability of the analysis. As mentioned earlier in this thesis, the detailed information for the L-PBF process such as temperature distribution and fluid flow in the melt pool shows the formation mechanism of the melt pool morphology.

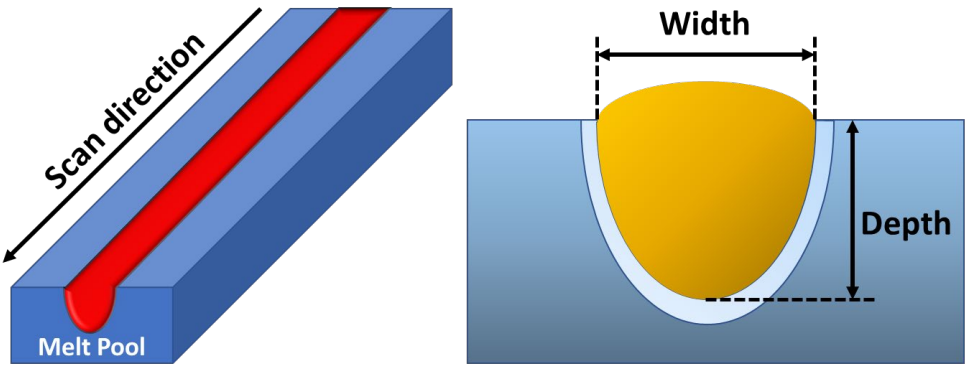


Figure 19. Illustration of Single-Track Deposition and Melt Pool Geometry

Since the proposed model contains various empirical models to describe the motion of fluid and heat transfer phenomena in the melt pool, it is required to calibrate some of the coefficients in those equations. One of these coefficients is the electrical conductance coefficient in the Fresnel reflection model. Since energy absorbed by the material dominates the thermo-fluid interaction, it can be regarded as the most important factor for predicting a melt pool dimension. As mentioned in Section 3.2, the electrical conductance coefficient $\varepsilon$ is highly dependent on not only the material properties of powder material but also the type of the laser and its power. Another value to be calibrated is the effective laser radius which determines the actual size of the beam acting on the surface of the melt pool. Therefore, in this thesis, a simple parametric study was conducted to estimate the proper effective radius of the laser beam and the electrical conductance coefficient. The calibrated effective beam radius was 42.4μm, and conductance coefficients for 50W, 100W, 150W, and 195W were 0.12, 0.12, 0.18, and 0.20, respectively.

Table 2. Laser Beam and Absorptivity Parameter

| Effective Beam Radius | Electrical Conductance Coefficient | | | |
|---|---|---|---|---|
| | 50W | 100W | 150W | 195W |
| 42.4μm | 0.12 | 0.12 | 0.18 | 0.20 |

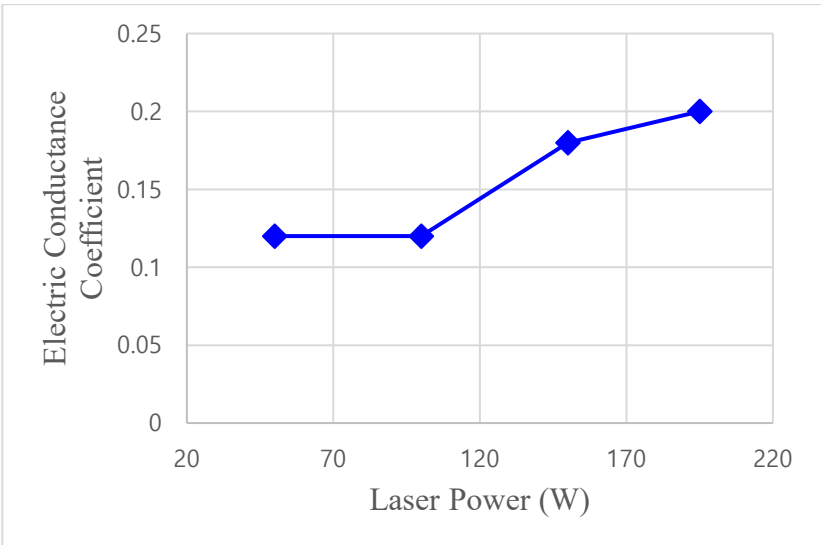


Figure 20. Electrical Conductance Coefficient with Different Laser Power

Interesting thing about the calibration values of the electrical coefficient is that they depended on the power of the laser. It seems obvious because laser properties representing its frequency is considered during the calculation of the electrical conductance coefficient. Typical laser such as Nd: YAG laser controls its power by altering the pulse period. Generally, the shorter pulse period produces the higher laser power, which increases the electrical conductance coefficient simultaneously. Furthermore, the increased value of the electrical conductance coefficient means escalated absorptivity of the base material. Therefore, it can be suggested that

the laser power and the relation of absorptivity of material would show similar relation as depicted in Figure 20. Generally, this s-curved relationship agrees with the findings proposed by Trapp et al [31].

The predicted sizes of the melt pool with the calibrated coefficients for different processing parameters were compared with the experimental values in Figure 22 and Figure 23. The shapes of the melt pool characterized by their depth and width in the simulation showed good agreement with the experimental values conducted by Dilip et al[32].

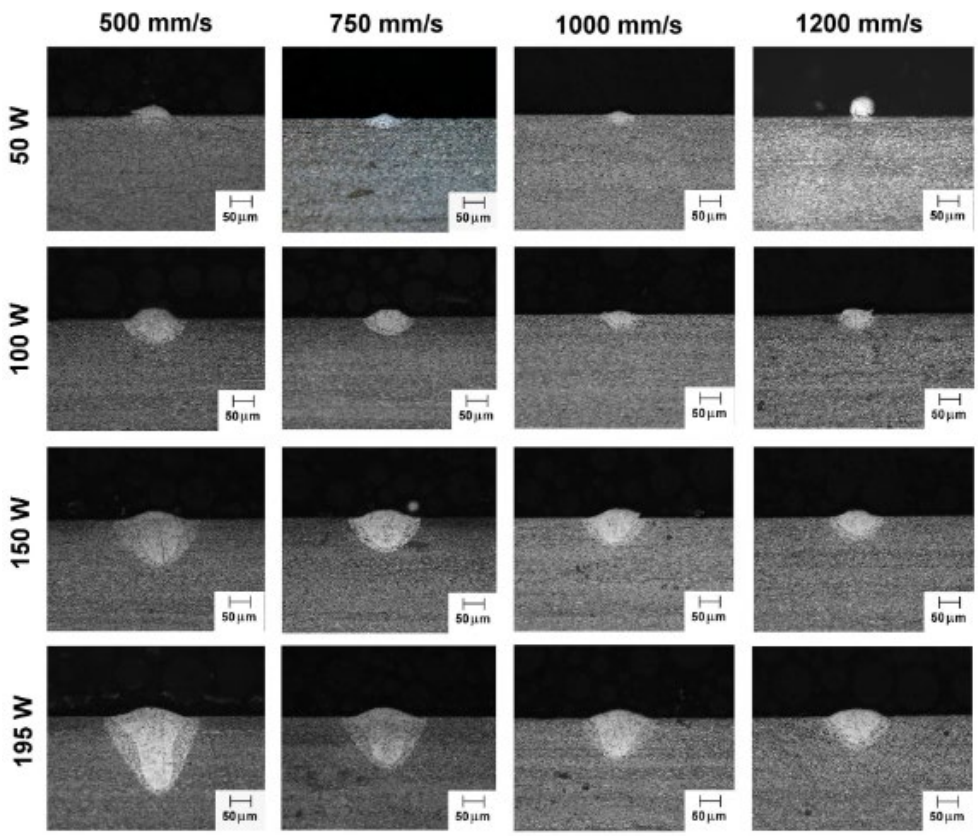


Figure 21. Cross sectional View of the Melt Pools with Different Process Parameters [32]

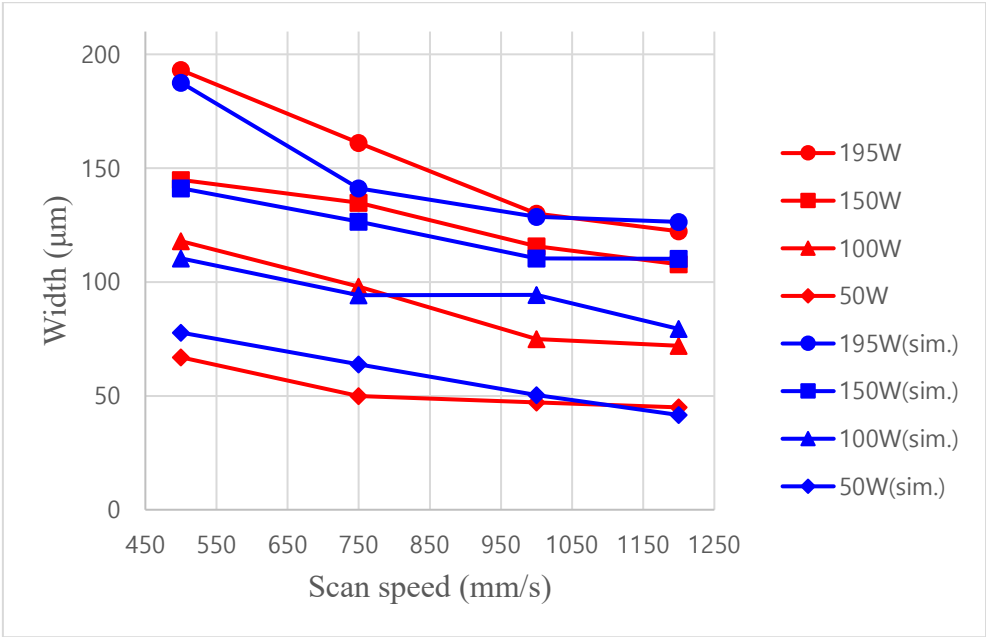


Figure 22. Melt Pool Width with Different Scan Speed

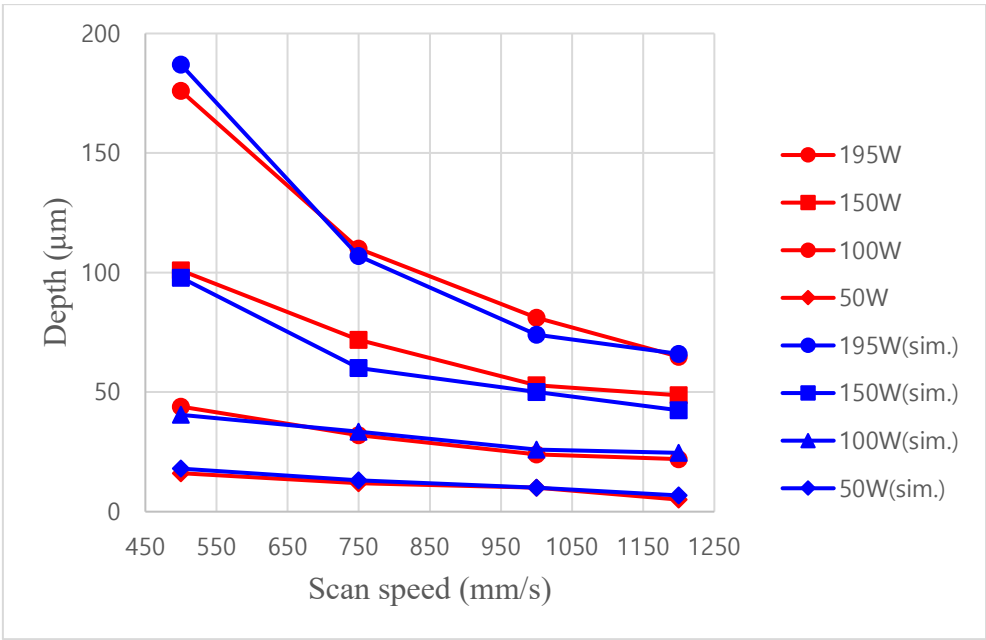


Figure 23. Melt Pool Depth with Different Scan Speed

Table 3. Absolute Error of Width Between Simulation and Experiment

| Absolute Error of Width Prediction | | | | |
|---|---|---|---|---|
| Laser Power | Scanning Velocity | | | |
| | 500 | 750 | 1000 | 1200 |
| 195 | 5.499 | 19.97 | 1.459 | 4.121 |
| 150 | 3.663 | 8.240 | 5.356 | 2.413 |
| 100 | 7.574 | 3.813 | 19.396 | 7.399 |
| 50 | 10.85 | 13.80 | 3.339 | 3.352 |

Table 4. Absolute Error of Depth Between Simulation and Experiment

| Absolute Error of Depth Prediction | | | | |
|---|---|---|---|---|
| Laser Power | Scanning Velocity | | | |
| | 500 | 750 | 1000 | 1200 |
| 195 | 11.05 | 3.062 | 7.077 | 1.176 |
| 150 | 3.009 | 11.74 | 2.847 | 6.264 |
| 100 | 3.438 | 1.386 | 2.054 | 2.618 |
| 50 | 1.910 | 1.152 | 0.0203 | 1.741 |

The maximum absolute errors for the width and depth were 19.97 μm (100W, 1000mm/s) and 11.74 μm (150W, 750mm/s), respectively. Also, the mean absolute errors were calculated as 7.515 μm and 3.784 μm for both width and depth.

As depicted in Figure 22 and Figure 23, it is obvious that the depth and width of the melt pool increase with the decrease in scanning speed when the laser power remains constant. On the other hand, with the fixed value of the scanning velocity, the deeper and wider melt pools were generated under increased energy input due to higher laser power. The graphical shapes of the melt region in single-track with no powder condition according to different process parameters are shown in Figure 24 and Figure 25. Overall, the calibrated coefficients and effective beam radius successfully captured the actual geometry of the melt pools. The detailed analysis of melt pool dynamics will be presented in the following section which deals the simulation with powder.

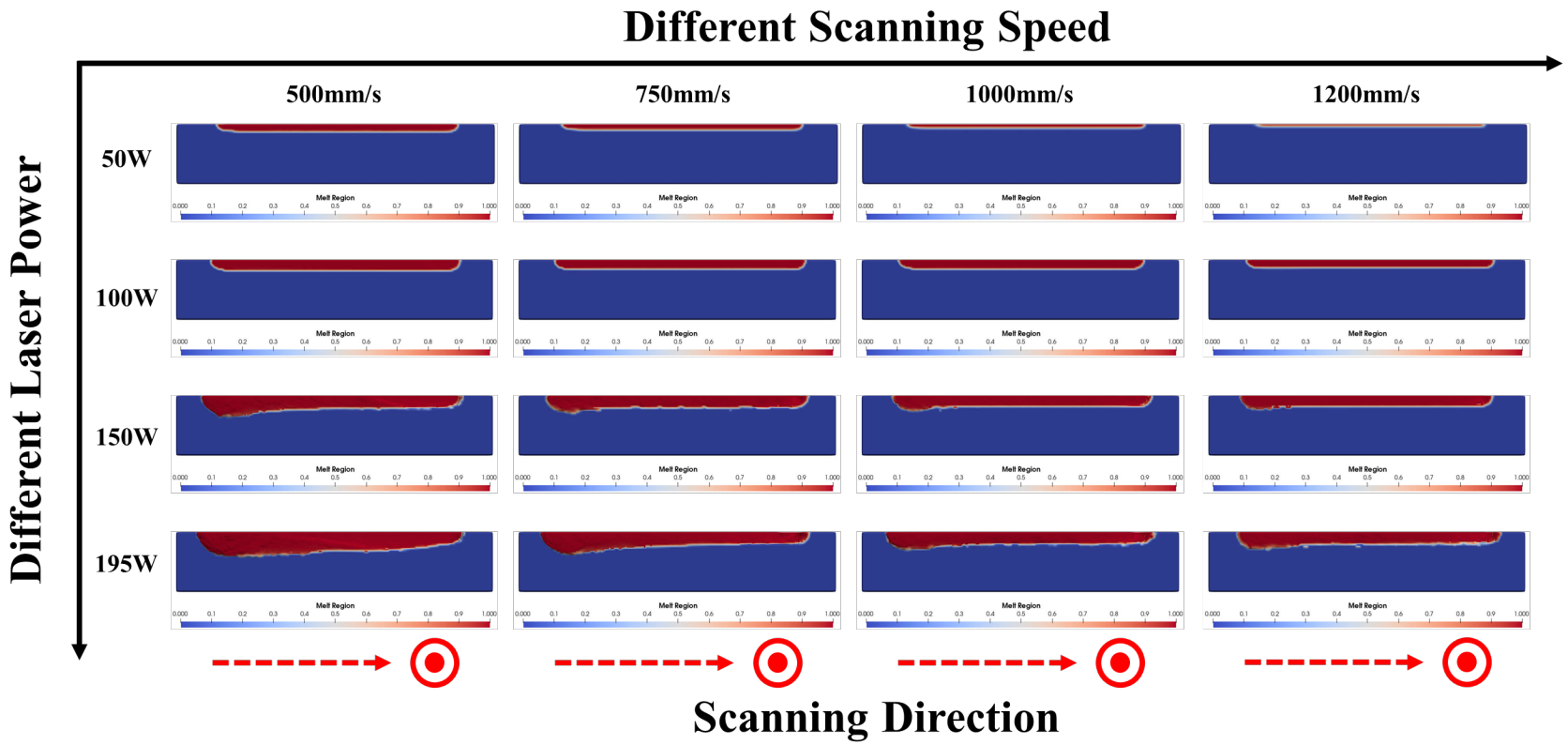


Figure 24. Influence of Process Parameters on the Melt Pool Geometry and Surface Morphology

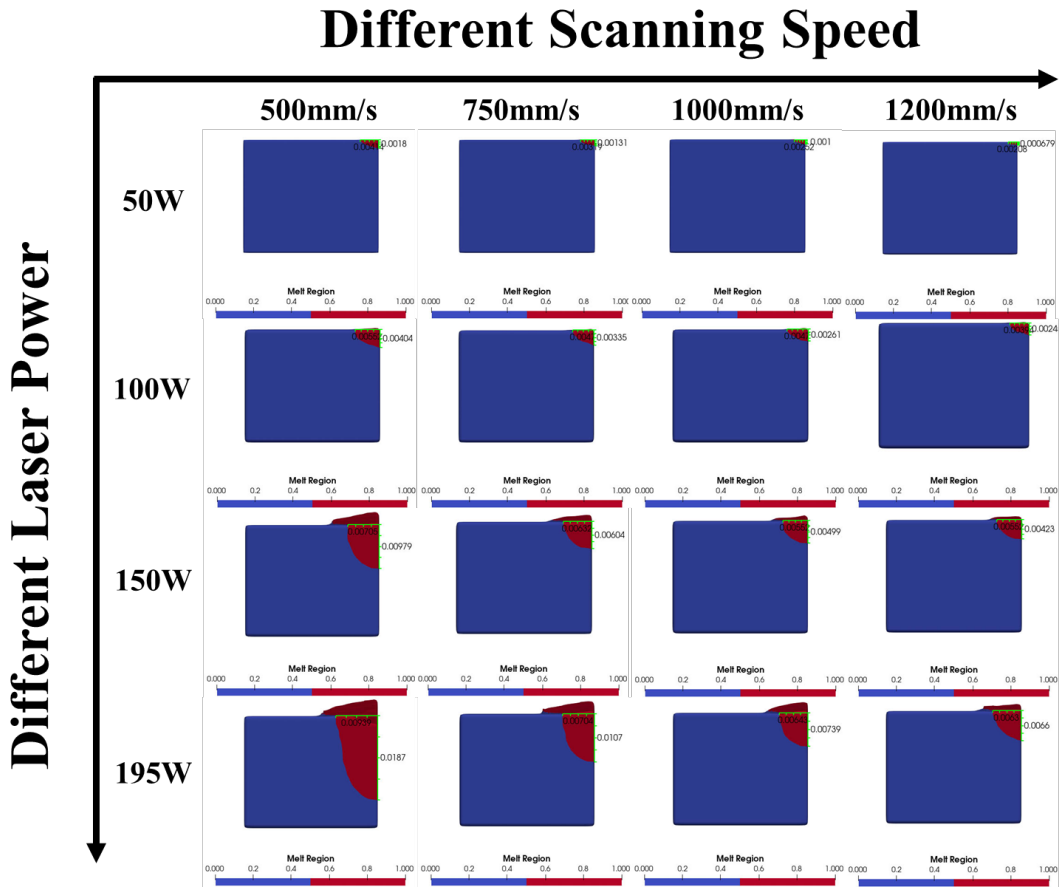


Figure 25. Influence of Process Parameters on the Melt Pool Size

## 4.2. Geometry and Morphology of the Melt Pool with Powder

The curves in Figure 26 show the change in the shape of the melt pool in the experiment and simulation with different laser power (scan speed maintained constant values of 500mm/s). As predicted before, the powder did not change the geometry of the melt pool dramatically. The depths and widths of the melt pool were well characterized with the calibrated value. The cross-sectional view of the melt pools and the surface morphologies of the whole track is shown in Figure 27.

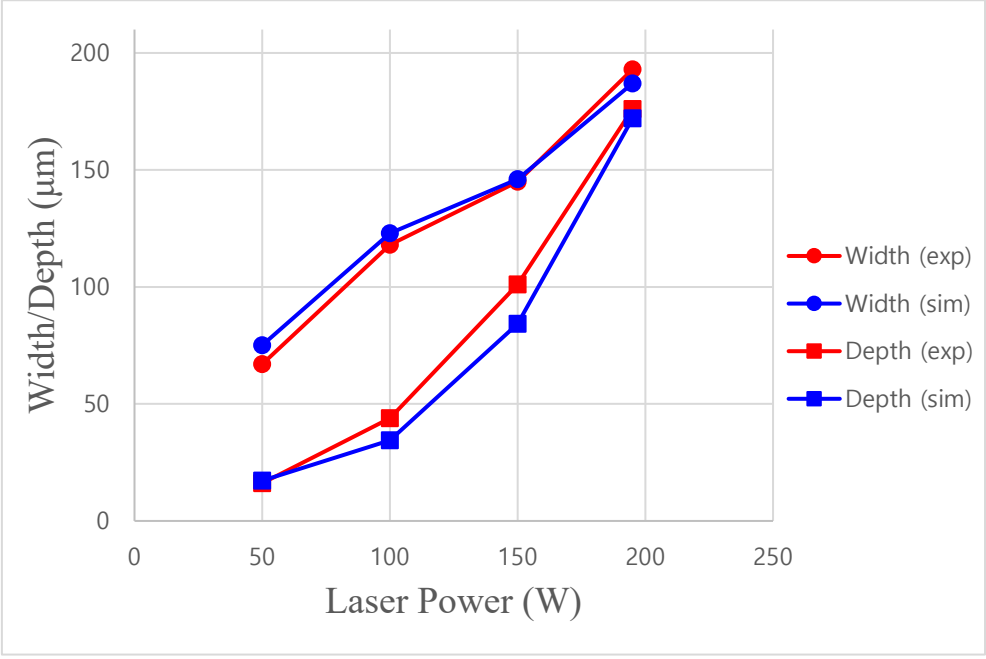


Figure 26. Comparison of Simulated Melt Pool Geometry and Experimental Results produced by Dilip et al[32]

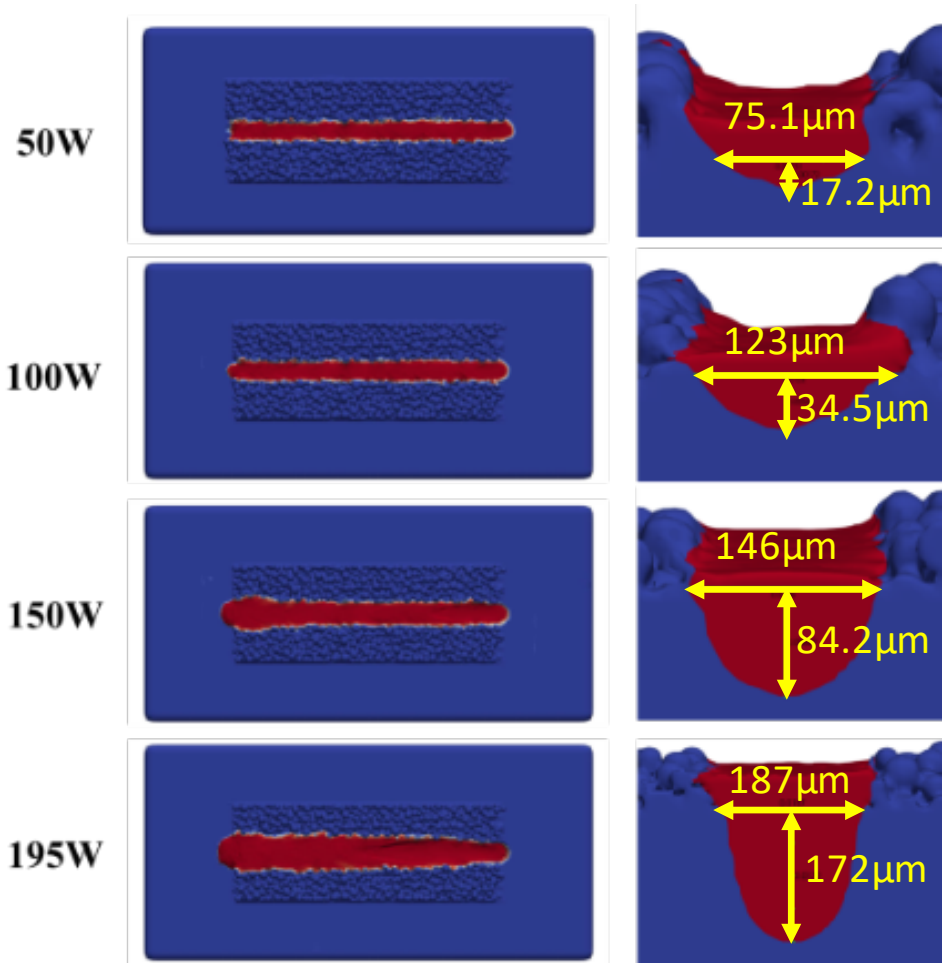


Figure 27. the Melt Pool Geometry and Surface Morphology of Single-track Simulation

Table 5. Percentage Error of Width and Depth Estimation

| Laser Power | Width Percentage Err. (Abs. Err.) | Depth Percentage Err. (Abs. Err.) |
|---|---|---|
| 50W | 12.09% (8.1μm) | 6.832% (1.1μm) |
| 100W | 4.237% (5μm) | 21.41% (9.4μm) |
| 150W | 0.690% (1μm) | 16.63% (16.8μm) |
| 195W | 3.109% (6μm) | 2.273% (4μm) |

## 4.3. Fluid Flow of the Melt Pool with Powder

Based on the fluid-dynamic relationship, the depth and width are highly dependent on the temperature distribution which is the result

of the fluid flow. Again, the fluid flow in molten metal is dominated by the combination of process parameters such as laser power and scanning speed.

The melting of powder during L-PBF was caused either by direct energy input by the laser rays or a hot return flow (shown in Figure 28) formed due to the negative pressure gradient present on the laser spot. As the powder melts, they obtained high flowability which allows the powder to have high velocity. Due to the recoil pressure and the Marangoni effect and the incompressibility of the flow, a large pressure was formed on the front of the melting site. The presence of high pressure encouraged the hot molten metal flows backward which lead to widened melt pool width.

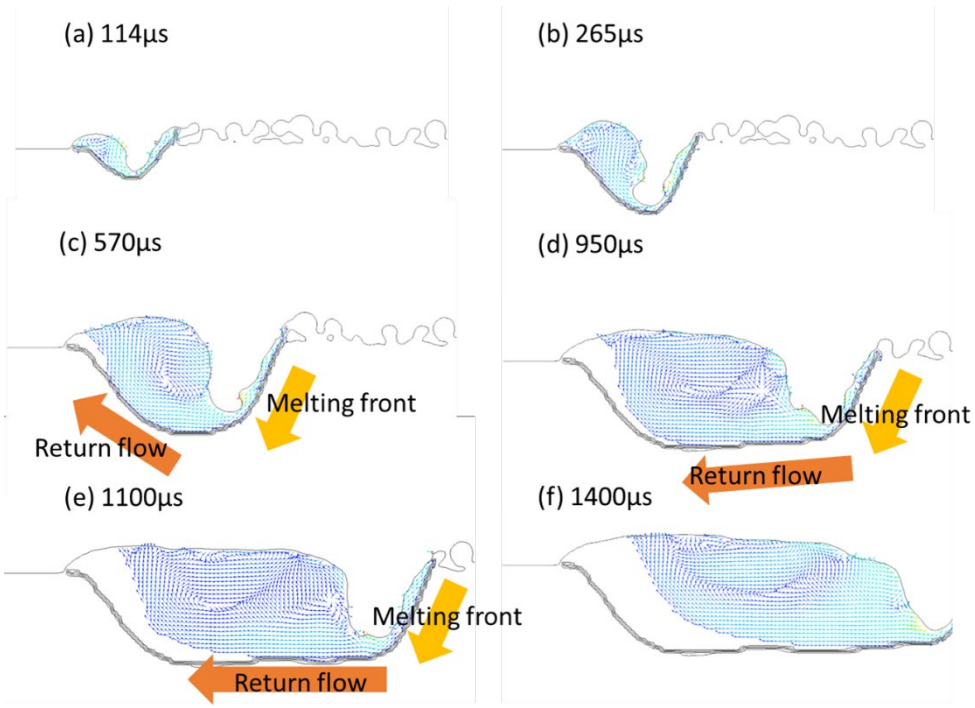


Figure 28. Melt Pool Contour and Velocity Vector during Scanning (195 W, 500 mm/s)

The forming process of melt pool is shown in Figure 29. At the early stage of the melt pool generation, the indentation was not generated because of the low heat accumulation, and the molten metal was flown toward the gap between powders. As a result, overall flow pattern was seemed to be chaotic compared to following stages. After few microseconds, backward flow was produced due to the evaporation pressure in front of the laser focusing area (Figure 29 yellow circle at 76μs). Accelerated backward flow with the combination of evaporation pressure, U shape indentation was continuously generated. Also, indentation was growing larger as heat accumulated. The acceleration of fluid was witnessed at the surface of the melt pool behind the U shape indentation. As shown in Figure 29, the backward flow slowed down as it approached to the surface due the drag. Once it reached to the surface right behind the U shape indentation, the flow accelerated to the backward. Since the temperature of the edge of the melt pool was much lower than the center of the melt pool, the surface tension would be much larger at the edge area. As a result, strong Marangoni effect was shown, and this backward acceleration was generated. Also, at the indented region, the steep wall was maintained without falling at 190 μs and 303 μs. Because of the reflected beam, the evaporation pressure was also generated at the side of the melt pool and pushed the wall not to fall. With the combination of above physical phenomena, the melt pool was grown until around 2200 μs. After 2200 μs, the volume of melt pool did not change dramatically and remain constant.

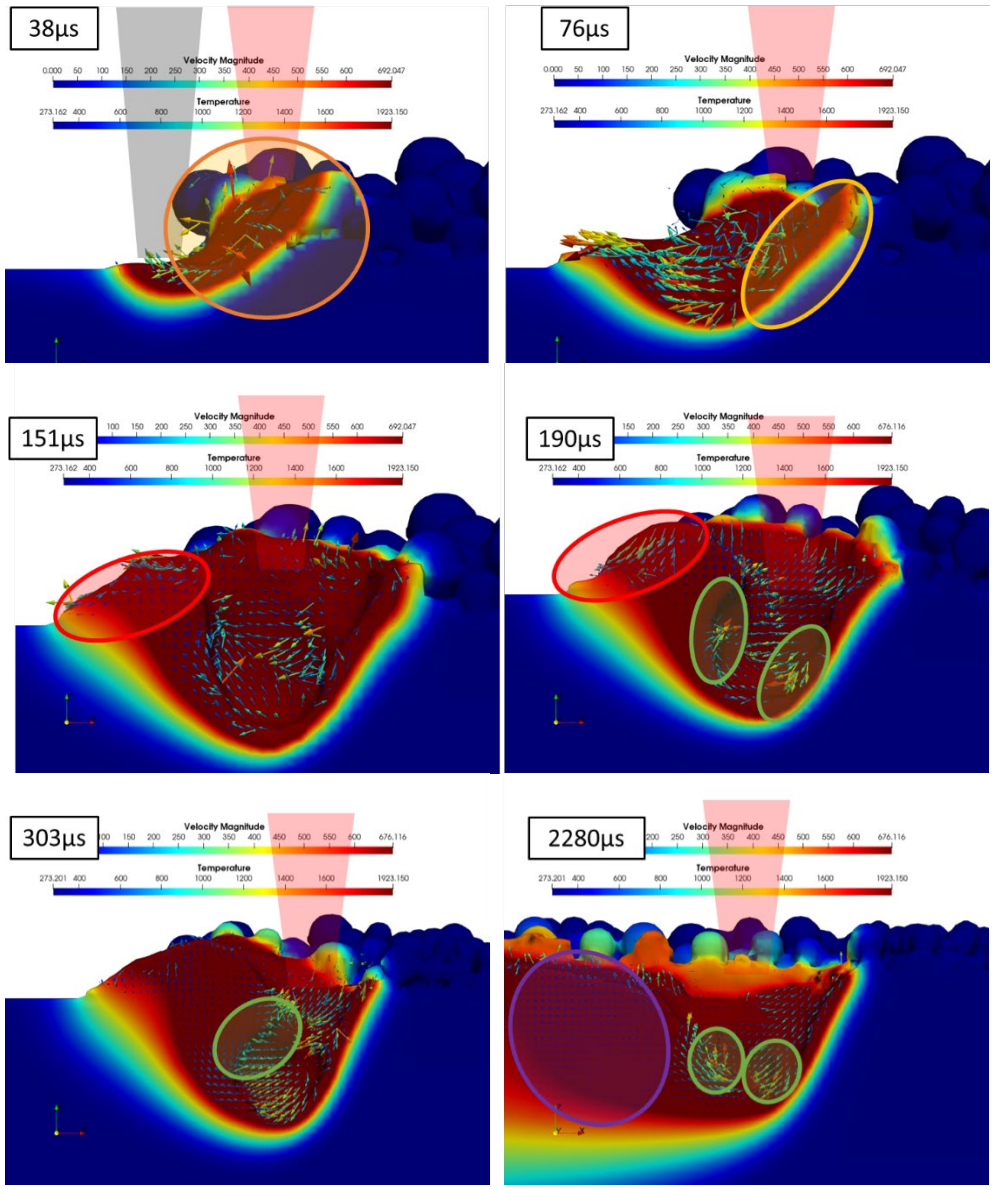


Figure 29. Temperature and 3D Velocity Vector during Process (195W, 500mm/s)

Figure 30 shows the vector of the fluid in melt pool at the scanning time of 760 μs with constant scanning velocity (500mm/s). When the laser power was set to be 195W, large area of surface was still in fluid phase and had high value of velocities. The maximum flow speed of 195W case was simulated as almost 2m/s which is fast

speed considering that the micrometer sized melt pool. Also, because of increased evaporation pressure, deep compression which is called keyhole was generated. At the bottom of the melt pool behind the laser spot, the bottom-up direction fluid flows were made, and flows marched back to the front near free surface.

In melt pool formed with 150W laser power, the similar backward flow was generated in front of the laser site. The backward flow, again, rose toward surface. Then affected by the Marangoni force, the fluid flowed to backward which had low temperature and high surface tension.

When the laser power was low enough (50W and 100W) to suppress the generation of keyhole, the surface fluid flowed only in a small area and the velocities of vectors were much smaller than other cases. There flow direction on the surface were relatively unpredictable due to the solid powder particle acted as a barricade. Also, the depths of the melt pool were comparably smaller than the 195W case. Moreover, comparing to other simulation cases, relatively unstable rugged boundary of melt pool was made for the 50W processing condition. What causes this craggy surface is not completely melted powder produced by the low laser power.

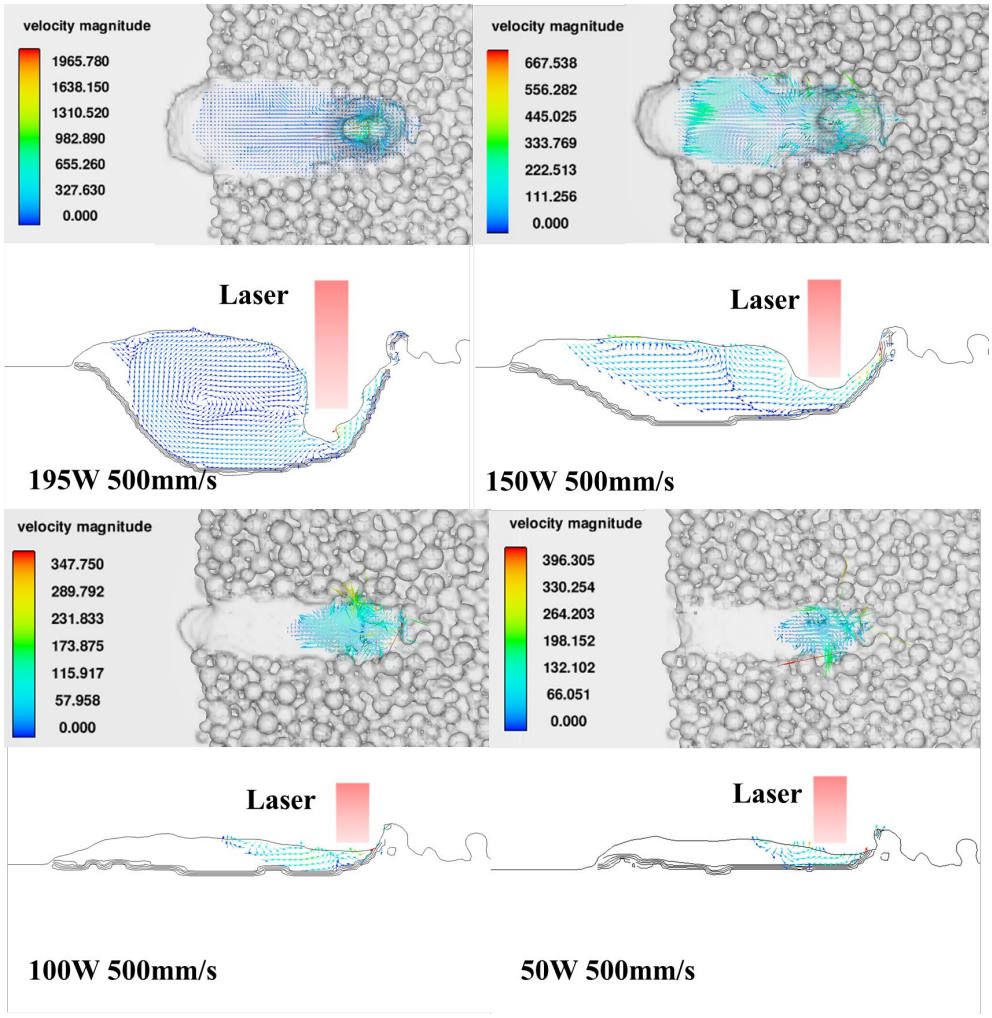


Figure 30. Fluid flow of the Melt Pool at the Time of 760 μs in Top View and XZ Plane View with Process Parameter of 50~195W with 500mm/s Scanning Speed

Temperature gradient as well as flow inside the melt pool plays important role in deciding the melt pool geometry. The temperature gradient time-dependent, so that it always changes due to the heat accumulation during the L-PBF process. Again, changed temperature gradient alters the corresponding fluid flow and melt pool geometry.

In the Figure 31, the evolution of the melt pool geometry during the single-layer/single-track scanning is given. As shown in the

figure, the dimension of the melt region firstly showed circular shape. However, as the lase moves, the shape of melt profile transferred to oval shape. Eventually, the geometry of melt region becomes comet shape as melt pool evolves.

When the circular shape of molten metal appeared, the flow direction was observed in all directions. Since the melt pool was surrounded by the solid state of the power particles, it seemed difficult to wet them. Due to the circular profile of melt pool, the fluid flows at side view follows the follows the U shape path, which was affected by the Marangoni convection force and the narrow unmelt region.

After some accumulation of heat, the powder particles near the high temperature were molten and flow in upward directions. At 600 μs, the bottom-up directional flow moved forward because solidified region blocked up the movement of the fluid flow. Also, the heat in the melt pool dissipated through thermal conduction to the powder bed, which hindered flow to penetrate into the deeper zone. After this point, the flow direction changed upward and solidified gradually, which slows down the fluid flow by the presence of the solidification drag. As the process progressed, the melt pool became deeper and longer with the continuous laser scanning process.

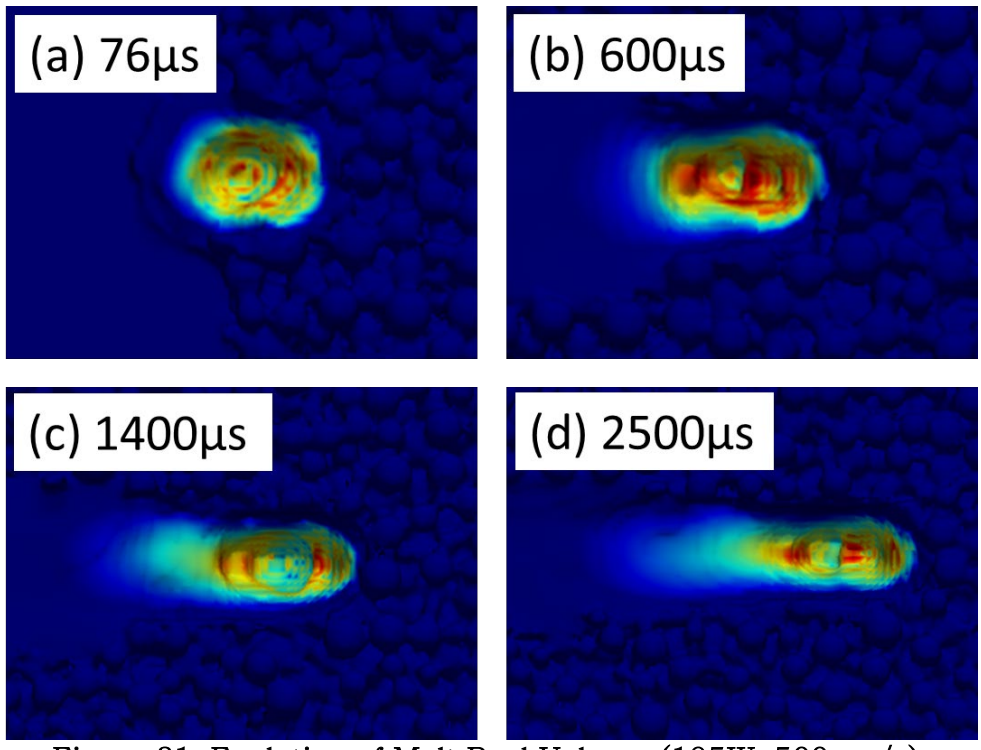

Figure 31. Evolution of Melt Pool Volume (195W, 500mm/s)

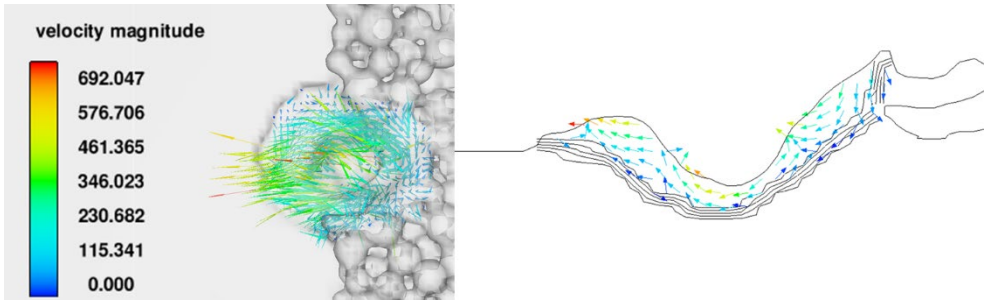

Figure 32. Flow Direction of Flow at 76 μs (195W, 500mm/s)

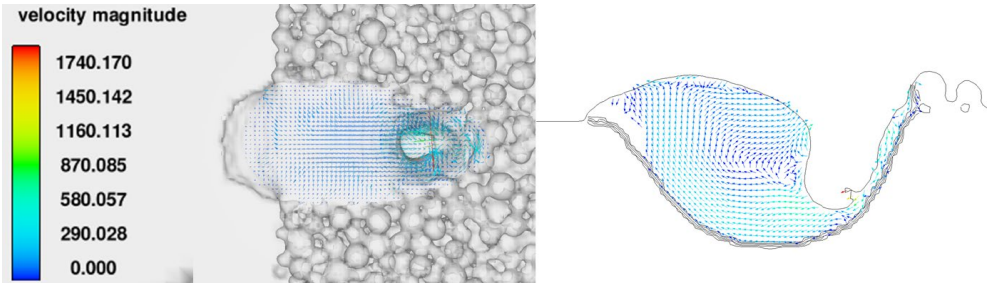

Figure 33. Flow Direction of Flow at 600 μs (195W, 500mm/s)

Figure 34 shows the solid fractions for the highest laser power case and 150W laser power case. As shown in the figure, with higher laser power, the melt pool grew faster and larger. However, it took a longer time to produce stabilized melt pool volume for the higher laser power.

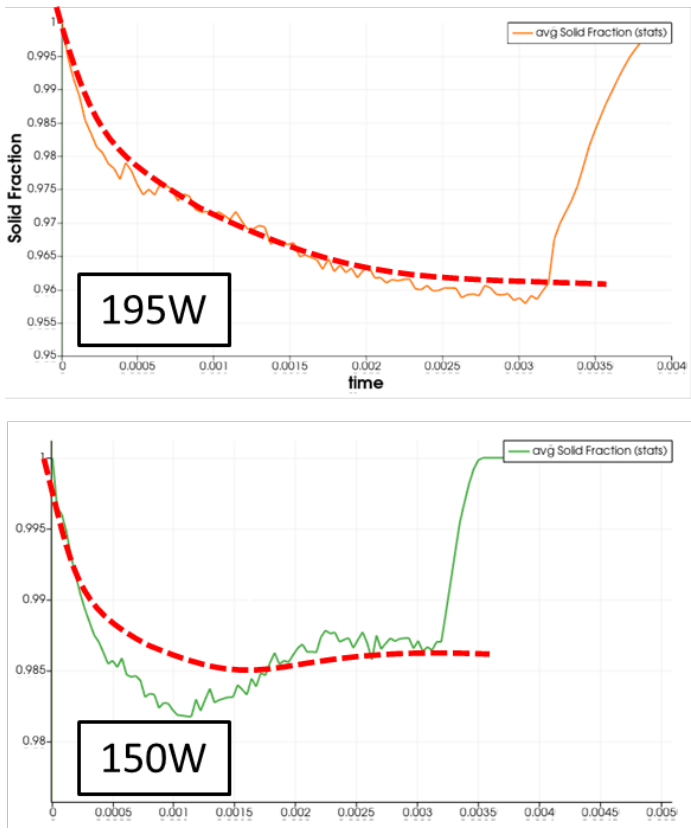


Figure 34. Solid Fraction During the Process

# Chapter 5. Conclusion and Future Work

## 5.1. Conclusions

In this thesis, multi-physics model containing multiphase flow, multiple reflection, recoil pressure, phase change including melting and solidifying, geometry-dependent absorptivity with ray-tracing, etc. with finite volume method is generated to capture the geometry and the free interface of the melt pool during the L-PBF fabricated Ti-6Al-4V. Based on the proposed model, firstly, the simulation without powder was conducted with some sets of the processing parameters for calibrating purpose. After calibrating, the single-track L-PBF process was simulated which is composed of two steps of simulation. Since it is required to geometry of the distributed particles, DEM simulation was conducted, and STL file was generated. Then the geometry was imported to the calibrated model. The simulated dimension of the melt pool geometries with selected processing conditions showed good agreement with the experimental values.

The results of this thesis provide some insight of fluid flow generation in the melt pool and their effect on the melt pool morphology. The geometry of melt pool which is determined by the width and the depth of the melt pool is significantly affected by the processing parameters such as laser power and scan speed. The input energy or hot return flow during the L-PBF process melts the powder and generates large negative pressure gradients in front of the spot zone. This kind of enormous pressure with the Marangoni

effect leads backward flow. Also, the presence of the heat accumulation induces the melt pool geometry circular to the elliptical and comet like shape at the end.

In this study, the limited number of numerical models considering powder geometry is computed due to high computational cost of L-PBF simulation with powder. However, to evaluate the validity of the proposed model with different scan speed and compare the effect of the scan speed on the generation of melt pool, additional numerical analysis is required. Furthermore, for the low power input conditions, it is better to increase the resolution of the FVM mesh. In this thesis, the size of meshes was 8 μm which can provide good numerical result with fast computing speed. However, 8 μm sized cell is not enough to capture the all the powders implemented in DEM simulation. As a result, the geometry of particle was slightly altered. Moreover, 8 μm mesh is too coarse to track the morphology of melt pool irradiated by low power laser.

## 5.1. Future Work

For the future work, additional simulation will be conducted to evaluate that whether the proposed model can predict the melt pool geometry with various scanning speed. Also, for attaining the grid independency, much finer mesh will be utilized.

In addition to supplementing of proposed model, the proposed model will be combined with reinforcing particle tracking algorithm.

Recently, the metal matrix composite is highlighted because of their outstanding mechanical properties compared to conventional additive manufacturing materials. Using reinforcing particles as nucleation sites, additive manufacturing can produce fine-grained equiaxed parts, so that one can acquire superior mechanical properties. However, coexistence of interactive phenomena which were mostly considered in this thesis with their short existence hinders the control of particle dispersion which is directly related to the final mechanical properties of MMC parts. Therefore, to the constructed numerical model, the Lagrangian discrete phase model will be implemented to track the particles in the melt pool.

# Reference

1.Tammas-Williams, S., et al., XCT analysis of the influence of melt strategies on defect population in Ti–6Al–4V components manufactured by Selective Electron Beam Melting. Materials Characterization, 2015. **102**: p. 47-61.

2.Kou, S., Welding metallurgy. New Jersey, USA, 2003. **431**(446): p. 223-225.

3.Ng, G.K.L., et al., Porosity formation and gas bubble retention in laser metal deposition. Applied Physics A, 2009. **97**(3): p. 641.

4.Xu, W., et al., Effects of processing parameters on fabrication defects, microstructure and mechanical properties of additive manufactured Mg–Nd–Zn–Zr alloy by selective laser melting process. Journal of Magnesium and Alloys, 2022.

5.Mostafaei, A., et al., Defects and anomalies in powder bed fusion metal additive manufacturing. Current Opinion in Solid State and Materials Science, 2022. **26**(2): p. 100974.

6.Zhao, C., et al., Real-time monitoring of laser powder bed fusion process using high-speed X-ray imaging and diffraction. Scientific Reports, 2017. **7**(1): p. 3602.

7.Bayat, M., et al., Keyhole-induced porosities in Laser-based Powder Bed Fusion (L-PBF) of Ti6Al4V: High-fidelity modelling and experimental validation. Additive Manufacturing, 2019. **30**.

8.Technologies, A.C.F.o.A.M. and A.C.F.o.A.M.T.S.F.o. Terminology, Standard terminology for additive manufacturing technologies. 2012: Astm International.

9.Sing, S.L., et al., 2 - 3D printing of metals in rapid prototyping of biomaterials: Techniques in additive manufacturing, in Rapid Prototyping of Biomaterials (Second Edition), R. Narayan, Editor. 2020, Woodhead Publishing. p. 17-40.

10.DebRoy, T., et al., Additive manufacturing of metallic components – Process,

structure and properties. Progress in Materials Science, 2018. **92**: p. 112-224.

11.Quintino, L. and E. Assunção, 6 - Conduction laser welding, in Handbook of Laser Welding Technologies, S. Katayama, Editor. 2013, Woodhead Publishing. p. 139-162.

12.Madison, J.D. and L.K. Aagesen, Quantitative characterization of porosity in laser welds of stainless steel. Scripta Materialia, 2012. **67**(9): p. 783-786.

13.Rai, R., et al., Heat transfer and fluid flow during keyhole mode laser welding of tantalum, Ti–6Al–4V, 304L stainless steel and vanadium. Journal of Physics D: Applied Physics, 2007. **40**(18): p. 5753-5766.

14.Brennan, M.C., J.S. Keist, and T.A. Palmer, Defects in Metal Additive Manufacturing Processes. Journal of Materials Engineering and Performance, 2021. **30**(7): p. 4808-4818.

15.Feng, S., et al., Experimental and numerical investigation of the origin of surface roughness in laser powder bed fused overhang regions. Virtual and Physical Prototyping, 2021. **16**(sup1): p. S66-S84.

16.Khairallah, S.A., et al., Laser powder-bed fusion additive manufacturing: Physics of complex melt flow and formation mechanisms of pores, spatter, and denudation zones. Acta Materialia, 2016. **108**: p. 36-45.

17.Sames, W.J., et al., The metallurgy and processing science of metal additive manufacturing. International Materials Reviews, 2016. **61**(5): p. 315-360.

18.Bontha, S., et al., Effects of process variables and size-scale on solidification microstructure in beam-based fabrication of bulky 3D structures. Materials Science and Engineering: A, 2009. **513-514**: p. 311-318.

19.Verhaeghe, F., et al., A pragmatic model for selective laser melting with evaporation. Acta Materialia, 2009. **57**(20): p. 6006-6012.

20.Dai, K. and L. Shaw, Distortion minimization of laser-processed components through control of laser scanning patterns. Rapid Prototyping Journal, 2002. **8**(5): p. 270-276.

21.Hodge, N.E., R.M. Ferencz, and J.M. Solberg, Implementation of a thermomechanical model for the simulation of selective laser melting. Computational Mechanics, 2014. **54**(1): p. 33-51.

22.Boley, C.D., S.A. Khairallah, and A.M. Rubenchik, Calculation of laser absorption by metal powders in additive manufacturing. Appl Opt, 2015. **54**(9): p. 2477-82.

23.Qiu, C., et al., On the role of melt flow into the surface structure and porosity development during selective laser melting. Acta Materialia, 2015. **96**: p. 72-79.

24.Khairallah, S.A. and A. Anderson, Mesoscopic simulation model of selective laser melting of stainless steel powder. Journal of Materials Processing Technology, 2014. **214**(11): p. 2627-2636.

25.Lee, Y.S. and W. Zhang, Modeling of heat transfer, fluid flow and solidification microstructure of nickel-base superalloy fabricated by laser powder bed fusion. Additive Manufacturing, 2016. **12**: p. 178-188.

26.Cho, J.-H. and S.-J. Na, Implementation of real-time multiple reflection and Fresnel absorption of laser beam in keyhole. Journal of Physics D: Applied Physics, 2006. **39**(24): p. 5372-5378.

27.Charles, A., et al., Elucidation of dross formation in laser powder bed fusion at down-facing surfaces: Phenomenon-oriented multiphysics simulation and experimental validation. Additive Manufacturing, 2022. **50**.

28.Ross, A.J., et al., Volumetric heat source calibration for laser powder bed fusion. Additive Manufacturing, 2022. **60**.

29.Liang, H., et al., The Size Effect on Forming Quality of Ti–6Al–4V Solid Struts

Fabricated via Laser Powder Bed Fusion. Metals, 2019. **9**(4).

30.Dezfoli, A.R., et al., Determination and controlling of grain structure of metals after laser incidence: Theoretical approach. Sci Rep, 2017. **7**: p. 41527.

31.Trapp, J., et al., In situ absorptivity measurements of metallic powders during laser powder-bed fusion additive manufacturing. Applied Materials Today, 2017. **9**: p. 341-349.

32.Dilip, J.J.S., et al., Influence of processing parameters on the evolution of melt pool, porosity, and microstructures in Ti-6Al-4V alloy parts fabricated by selective laser melting. Progress in Additive Manufacturing, 2017. **2**(3): p. 157-167.

# 국문초록

# Ti-6Al-4V 재료를 사용한 레이저 분말 베드 용융법 (L-PBF)에서의 다물리 모델링 구축과 용융풀 특성화

정 민 규

항공우주공학과

서울대학교 대학원

본 학위논문은 전산유체해석 (CFD)를 적용하여 L-PBF (레이저 분말 베드 용융법)을 사용한 금속 적층 제조 공정 중 생성되는 용융풀의 형태를 예측하는 방법에 관한 논문이다. L-PBF 방식의 적층제조는 가장 신뢰성 높은 금속 적층 방식의 한가지로, 마이크로미터 사이즈의 분말을 빌드 플레이트 위에 고르게 도포하고 용융과 응고를 반복하며 층을 쌓으며 부품을 제조하는 방법이다. 다른 금속 적층 제조 방식과 마찬가지로, L-PBF 방식은 엔지니어로 하여금 주조나 절삭과 같은 기존 생산 공정으로는 제조할 수 없는 복잡한 형상을 보다 쉽고 빠르게 설계 및 생산을 가능케 하였다. 또한 적층 제조 방식은 폐기물의 발생이 적어 보다 효율적인 생산이 가능하다. 이렇듯 L-PBF 방식에는 다양한 장점이 있지만, L-PBF 공정 중 발생하는 융합 부족 또는 키홀 등의 결함은 부품의 품질을 저해하는 요인이 되고 있다. 이러한 결함 생성의 원인을 파악하고 방지하기 위해서 용융풀 내에서 발생하는 유동 흐름에 대해 분석하는 과정이 필요하지만, L-PBF 과정 중에 일어나는 용융 및

응고는 매우 짧은 시간에 일어나므로 분석이 쉽지 않다. 더욱이 전도, 대류, 복사 등의 열전달이 동시에 일어나고, 기화와 같은 물질 전달도 같이 일어나는 등 복잡한 물리 현상이 결합되어 나타나 용융풀 내 유동의 거동을 파악하는데 어려움을 더하고 있다. 따라서 이러한 문제를 해결하기 위해 전산 해석이 활용될 수 있다. 본 논문에서는 다양한 공정 변수를 가지는 단일 트랙/단일 레이어 L-PBF 공정에 대한 다물리 모델을 구축하여 용융풀의 발생과 성장을 평가하는데 활용하였다. 구축된 다물리 모델에는 다상유동, 용융/응고, 전도/대류 등의 열전달, 모세관힘, 반발압력, 레이저 흡수율 등 다양한 물리 현상들이 반영되었다. 본 논문에서 구축된 모델을 통해 실험 결과와 유사한 용융풀 형상을 얻을 수 있었다. 또한 전산 해석 결과를 통해 레이저 출력과 레이저 스캔 속도가 용융풀 내의 유동에 지대한 영향을 미침과 동시에 용융풀의 형상에도 큰 영향을 미침을 확인할 수 있었다. 결과적으로, 본 연구는 L-PBF 중 발생하는 용융풀 내의 유동 메커니즘에 대한 보다 넓은 이해를 제공하였다.

**Keyword** : Additive Manufacturing, Selective Laser Melting, Melt Pool Characterizing, Computational Fluid Dynamics

**Student Number** : 2021-27248